J. Fluid Mech. (1997), *vol.* 349, *pp.* 253–293. Printed in the United Kingdom

Subgrid-scale stresses and their modelling in a turbulent plane wake

By JOHN O'NEIL† AND CHARLES MENEVEAU

Department of Mechanical Engineering, The Johns Hopkins University, Baltimore, MD 21218, USA

(Received 26 December 1996 and in revised form 5 June 1997)

Velocity measurements using hot wires are performed across a high-Reynolds-number turbulent plane wake, with the aim of studying the subgrid-scale (SGS) stress and its modelling. This quantity is needed to close the filtered Navier–Stokes equations used for large-eddy simulation (LES) of turbulent flows. Comparisons of various globally time-averaged quantities involving the measured and modelled SGS stress are made, with special emphasis on the SGS energy dissipation rate. Experimental constraints require the analysis of a one-dimensional surrogate of the SGS dissipation. Broadly, the globally averaged results show that all models considered, namely the Smagorinsky and similarity models, as well as the dynamic Smagorinsky model, approximately reproduce profiles of the surrogate SGS dissipation. Some discrepancies near the outer edge of the wake are observed, where the Smagorinsky model slightly overpredicts, and the similarity model underpredicts, energy dissipation unless the filtering scale is about two orders of magnitude smaller than the integral length scale.

A more detailed comparison between real and modelled SGS stresses is achieved by conditional averaging based on particular physical phenomena: (i) the outer intermittency of the wake, and (ii) large-scale coherent structures of the turbulent wake. Thus, the interaction of the subgrid scales with the resolved flow and model viability can be individually tested in regions where isolated mechanisms such as outer intermittency, vortex stretching, rotation, etc., are dominant. Conditioning on outer intermittency did not help to clarify observed features of the measurements. On the other hand, the large-scale organized structures are found to have a strong impact upon the distribution of surrogate SGS energy dissipation, even at filter scales well inside the inertial range. The similarity model is able to capture this result, while the Smagorinsky model gives a more uniform (i.e. unrealistic) distribution. Both dynamic Smagorinsky and similarity models reproduce realistic distributions, but only if all filter levels are contained well inside the inertial range.

1. Introduction

In large-eddy simulation (LES) of incompressible turbulent flow one seeks solutions to the filtered Navier–Stokes equations, which requires the subgrid-scale (SGS) stress tensor to be parameterized as function of the resolved velocity field. The SGS tensor is defined according to

$$\tau_{ij} \equiv \widetilde{u_i u_j} - \widetilde{u}_i \widetilde{u}_j, \tag{1}$$

† Present address: Applied Physics Laboratory, Laurel, MD 20723–6099, USA.

where the tilde represents spatial filtering at a scale Δ. There is a significant body of literature on the subject of SGS modelling for LES, e.g. Lilly (1967), Deardorff (1970), Leonard (1974), Kraichnan (1976), Bardina, Ferziger & Reynolds (1980). Comprehensive reviews are given in Rogallo & Moin (1984) and, more recently, Lesieur & Métais (1996). The SGS stress τ_{ij} is a strongly fluctuating variable whose basic properties and its relationship with the large scales of the flow must be understood in order to formulate accurate parameterizations.

Given a fully resolved field, the stress can be computed according to its definition, equation (1). This allows SGS stresses computed by filtering fully resolved turbulent fields to be compared with model expressions also evaluated from resolved velocity fields (Clark, Ferziger & Reynolds 1979; Piomelli, Moin & Ferziger 1988). Such *a priori* studies of SGS modelling have, in the past, concentrated mainly on isotropic turbulence (e.g. Clark *et al.* 1979; Domaradski, Liu & Brachet 1993), and planar channel flow (e.g. Piomelli *et al.* 1988; Härtel *et al.* 1994). The data were mostly obtained from direct numerical simulation (DNS) at low Reynolds number ($R_\lambda \sim 100$). Experimental data at higher Reynolds numbers ($R_\lambda \sim 300$) have also been analysed for the purpose of *a priori* studies (Liu, Meneveau & Katz 1994). There, two-dimensional particle-image-velocimetry (PIV) measurements were performed in the far field of a round jet about the jet axis, where the turbulence statistics are not far from homogeneous. Hot-wire measurements in grid turbulence ($R_\lambda \sim 150$) were analysed in Meneveau (1994). Several conclusions have been reached from such *a priori* studies. Among them has been the realization that on an instantaneous basis the eddy-viscosity closures do not properly reproduce the real stresses, while the similarity models (to be described in detail below) yield more realistic distributions. However, on average the traditional eddy-viscosity models were shown to predict the correct rate of energy dissipation in turbulent regions away from walls. Measured model coefficients agreed approximately with traditional values. Quite importantly, it was shown based on the data that the dynamic procedure (Germano *et al.* 1991) is able to extract such coefficients from information contained in the resolved scales.

The motivation for the present study is to extend such experimental *a priori* studies to include more of the flow complexities typically encountered in turbulent shear flows. In particular, we wish to capture effects of non-homogeneity of flow statistics on properties of the SGS stress. In addition to average spatial non-homogeneity, free shear flows are characterized by several important features of the instantaneous fields. Among these are outer intermittency, the coexistence of turbulent and irrotational flow near the shear layer's edges, and the existence of well-defined large-scale coherent structures. One would like to know how the real SGS stress τ_{ij}, the models, and other variables of interest for LES, respond to the presence of such phenomena at high Reynolds numbers. Outer intermittency and large-scale coherent structures are not ubiquitous in grid turbulence or fully developed channel flows, and were not available from the PIV data in the inner portion of the far-field jet studied in Liu *et al.* (1994).

In this study we focus on the planar wake behind a circular cylinder. Measurements will be performed across a significant portion of the wake, in order to capture the spatial non-homogeneity of this flow. The wake includes the phenomena of outer intermittency, as well as large-scale coherent structures.

A primary issue concerns characterizing fundamental features of the SGS stress and the applicability of different SGS models. One approach is to examine features of an instantaneous realization of real and modelled fields, e.g. the SGS dissipation field. The comparison can be based on the correlation coefficient of the actual and modelled SGS dissipation across the field. While much can be learned from this approach, partial

agreement of local instantaneous features does not provide a sufficient (or necessary) condition for the proper modelling of the subgrid scales. Another possibility is to compare mean values, by averaging over very long times. Agreement between certain averaged quantities can be shown to yield *necessary* conditions (Meneveau 1994) that a model should reproduce. However, a few average values contain only limited information about the SGS stress. To completely describe turbulence subgrid scales and the models with statistics requires, in principle, an infinite number of multipoint joint moments.

A more focused comparison based on isolated physical mechanisms can be made by conditional averaging. As mentioned before, an important phenomenon in the wake is outer intermittency, consisting of the coexistence of turbulent and irrotational flow, especially at the wake's edges (Corrsin & Kistler 1955). Another important phenomenon in this flow is the presence of large-scale coherent structures. There has been a large body of work documenting the existence of coherent structure in canonical shear flows, and in the cylinder wake in particular (Hussain & Hayakawa 1987; Cantwell 1981). Instead of only calculating global averages, one may use coherent structure and/or outer intermittency, and conditionally average on these phenomena to disentangle different large-scale flow phenomena, and study properties of the SGS stress and models under such more clearly defined conditions.

In a recent DNS study of channel flow, Piomelli, Yu & Adrian (1996) used the SGS dissipation as a criterion for conditional averaging. Conditional flow structures were obtained whenever the local SGS dissipation exceeded a positive (or negative) value. They concluded that the interscale energy transfer is highly correlated with the presence of structures. If this feature is a general property of the relationship between large-scale coherent structures and SGS dynamics, then the assumption of universality of small-scale motion may be less justified. We will examine this issue in the context of the plane wake. In this flow, the most ubiquitous large-scale coherent structures are the vortices in the Kármán-vortex street. They are visible in the near and so-called intermediate field, maybe up to 30 diameters downstream of the cylinder, even at very large Reynolds numbers. Those large-scale structures are characterized by different regions, ranging from vortex cores to highly strained saddle points.

In order to accurately measure conditional averages, extensive data must be available at every sampling point. This can be accomplished by using traditional thermal anemometry. Of course hot-wire data are severely limited compared to more recent multidimensional measurement techniques such as particle image velocimetry (Adrian 1991; Liu *et al.* 1994), in the sense that Taylor's hypothesis must be used, and that it gives only one-dimensional sections through the flow. On the other hand, very long data records required for converged statistics can be obtained at selected points with hot wires, which is still difficult when using PIV.

Arguably the most important feature of the subgrid-scale stress is how it affects the kinetic energy of the resolved field. Thus, energy dissipation arising from the interactions between subgrid and resolved scales is the main focus of this study. In order to more concretely formulate the questions to be addressed, the concept of SGS energy dissipation is briefly reviewed below. This is followed by a review of the basic models to be considered.

1.1. *Subgrid-scale energy dissipation*

The SGS stress tensor has profound effects on the energetics of the resolved flow field, as can be deduced from the resolved kinetic energy equation (see e.g. Piomelli *et al.*

1991):

$$\frac{\partial \frac{1}{2}\widetilde{q}^2}{\partial t} + \widetilde{u}_j \frac{\partial \frac{1}{2}\widetilde{q}^2}{\partial x_j} = -\frac{\partial}{\partial x_j}\left(\frac{1}{\rho}\widetilde{p}\widetilde{u}_j + \tau_{ij}\widetilde{u}_i - 2\nu\widetilde{u}_i\widetilde{S}_{ij}\right) - 2\nu\widetilde{S}_{ij}\widetilde{S}_{ij} + \tau_{ij}\widetilde{S}_{ij} + \widetilde{f}_i\widetilde{u}_i, \quad (2)$$

where the resolved kinetic energy field is defined as

$$\tfrac{1}{2}\widetilde{q}^2 \equiv \tfrac{1}{2}\widetilde{u}_i\widetilde{u}_i, \quad (3)$$

and $\widetilde{S}_{ij} \equiv \frac{1}{2}\left(\partial\widetilde{u}_i/\partial x_j + \partial\widetilde{u}_j/\partial x_i\right)$ is the resolved strain-rate tensor. The first term on the right-hand-side of (2) represents spatial transport, which vanishes on average for homogeneous flows. The second is direct dissipation due to molecular viscosity. At high Reynolds numbers, away from no-slip boundaries, this term is quite small. The third term, $\tau_{ij}\widetilde{S}_{ij}$, is the so-called SGS dissipation rate, and typically has a negative average value, representing a net drain of resolved kinetic energy into unresolved motion. The last term represents energy injection (or extraction) by body forces. One concludes that on average, in the inertial range, the SGS dissipation term represents the most important effect of the unresolved scales on the evolution of kinetic energy of the resolved field. Therefore, most attention will be devoted to this particular statistic of the SGS stress.

1.2. *Smagorinsky model*

Since the inception of LES, the eddy-viscosity model first formulated by Smagorinsky (1963) remains in wide use. The model for the deviatoric part of the stress is

$$\tau_{ij}^d = -2\left(C_S\Delta\right)^2 \left|\widetilde{S}\right|\widetilde{S}_{ij}, \quad (4)$$

where the modulus of the resolved strain rate is

$$\left|\widetilde{S}\right| \equiv (2\widetilde{S}_{mn}\widetilde{S}_{mn})^{1/2}. \quad (5)$$

C_S is a dimensionless coefficient. Given the dynamical importance of SGS energy dissipation, a strategy to determine, or calibrate, C_S from data is to require that the Smagorinsky model reproduces the correct mean SGS dissipation. This leads to

$$C_S^2 = -\frac{\left\langle \tau_{ij}\widetilde{S}_{ij}\right\rangle}{\left\langle 2\Delta^2\left|\widetilde{S}\right|\widetilde{S}_{mn}\widetilde{S}_{mn}\right\rangle}. \quad (6)$$

The averaging can be ensemble, time, or spatial, depending on specific flow conditions.

The coefficient determined by condition (6) (and similar ones for models discussed later) can be interpreted as follows: using this value in LES is a necessary condition to reproduce the correct SGS dissipation assuming that the simulation is producing the correct value of the denominator $2\left\langle\Delta^2\left|\widetilde{S}\right|\widetilde{S}_{mn}\widetilde{S}_{mn}\right\rangle$ (see §3.4 for a more detailed discussion of this issue).

The Smagorinsky model implicitly assumes that the subgrid scales adjust instantaneously to changes in the resolved field. By construction, the model is dissipative, and only allows for forward transfer of energy from the resolved scales to the unresolved ones. Among others, Piomelli *et al.* (1991) and Liu *et al.* (1994) have found both of these features to be unrealistic.

1.3. *Similarity model*

The similarity models form a different class of parameterization (Bardina *et al.* 1980; Liu *et al.* 1994). They take advantage of the high correlation observed between the

smallest resolved scales and the actual SGS scales, which leads to

$$\tau_{ij} = C_L L_{ij}, \tag{7}$$

where

$$L_{ij} \equiv \overline{\widetilde{u}_i \widetilde{u}_j} - \overline{\widetilde{u}_i}\,\overline{\widetilde{u}_j}. \tag{8}$$

The overline denotes a second filtering operation, typically at a scale 2Δ. Originally (Bardina *et al.* 1980) this was performed at the same level as the grid filter, Δ, but it was later found to be more appropriate to filter at larger lengths (Liu *et al.* 1994). By construction, this model assumes that the local stresses at different filter levels are very similar, so a similarity coefficient $C_L \sim O(1)$ is to be expected. As was done for the Smagorinsky coefficient, one may contract the SGS stress and model with $\widetilde{S}_{ij}$ to form the SGS dissipation, and again solve for the coefficient according to

$$C_L = \frac{\langle \tau_{ij} \widetilde{S}_{ij} \rangle}{\langle L_{mn} \widetilde{S}_{mn} \rangle}. \tag{9}$$

In simulations, the model is typically supplemented with the Smagorinsky model (mixed model) to ensure that mean dissipation of kinetic energy takes place in the simulation (Zang, Street & Koseff 1993; Vreman, Guerts & Kuerten (1994); etc.). The similarity term then accounts for more local features of the flow, such as backscatter (Liu *et al.* 1994; Piomelli *et al.* 1996).

1.4. *Dynamic Smagorinsky model*

In the traditional Smagorinsky model, the coefficient C_S needs to be prescribed *a priori*. This is a serious drawback since different regions of the flow may require different coefficient values. For instance, if one is modelling subgrid scales in the presence of a turbulent/non-turbulent interface, which typically bounds shear flows, one may need to reduce the coefficients in the outer, non-turbulent regions. Germano *et al.* (1991) carried the idea of similarity between scales to the next logical step by introducing the dynamic Smagorinsky model

$$\tau_{ij}^d = -2\,(C_{SD}\Delta)^2\,|\widetilde{S}|\widetilde{S}_{ij}, \tag{10}$$

where the coefficient is obtained from

$$C_{SD}^2 = \frac{\langle L_{ij} M_{ij} \rangle^*}{\langle M_{mn} M_{mn} \rangle^*}. \tag{11}$$

L_{ij} was defined in (8), and M_{ij} is defined as

$$M_{ij} = -2\left((2\Delta)^2 |\overline{\widetilde{S}}|\overline{\widetilde{S}}_{ij} - \Delta^2 \overline{|\widetilde{S}|\widetilde{S}_{ij}}\right). \tag{12}$$

The averaging operation $\langle\ \rangle^*$ is required to avoid very small denominators or negative numerator values in (11), which tend to produce numerical instabilities when implemented without averaging. The averaging is performed over regions of statistical homogeneity (Germano *et al.* 1991; Ghosal *et al.* 1995) or fluid pathlines (Meneveau, Lund & Cabot 1996).

There are other variants of the eddy-viscosity and similarity models, but in order to keep the discussion focused, this work will address the regular and dynamic Smagorinsky and similarity models in the basic forms outlined above.

1.5. *Outline*

Details of the experimental setup, instrumentation, measurements performed, and basic flow characteristics are presented in § 2. Plane wakes are characterized by a slow downstream development of mean quantities. While much is known about the distributions of Reynolds-averaged Navier–Stokes (RANS) variables, very little is known about the spatial distribution of mean LES variables in the plane wake. Section 3 describes basic aspects of the data analysis procedures such as filtering, and key assumptions used. Section 4 describes systematic profile measurements across the wake, from $x/D = 25$ to $x/D = 100$, where D is the cylinder diameter. The focus there is on documenting the spatial distribution of variables such as the time-averaged SGS dissipation rate, model coefficients obtained according to (6) and (9), correlation coefficients between real and modelled stress elements, effects of filter scale, etc.

As one spans different axial and transverse locations inside the wake, the mean shear, fluctuating strain, and other quantities vary significantly. If one were to perform LES using the traditional Smagorinsky or similarity model, a constant coefficient for all locations in the field would be employed. Thus, a measure of how well or how poorly such models capture the mean SGS dissipation is the degree of spatial variation the coefficients (measured according to (6) and (9)) exhibit throughout the wake. If there are variations, one is interested to find out whether the dynamic procedure allows one to capture such variations.

Another interesting issue arises because the dynamic and similarity models involve several different filter levels, and assume that the coefficient is the same at the different filter levels. As one moves to the limits of the inertial range (say if $\Delta \rightarrow L$, where L is the integral scale), this assumption may begin to be questionable, and at lower Reynolds numbers, where the inertial range disappears, this assumption may become invalid. What are the implications of these possible limitations on the similarity model, or on the dynamic model? This is a practically important question as LES is often done with very coarse grids (VLES) so that the inertial range is not captured. Section 4 also includes a study of the effects of Reynolds number.

To ascertain if transverse variations of the Smagorinsky coefficient are due to outer intermittency, conditional averaging is performed in order to distinguish between turbulent and non-turbulent regions (see §5).

Section 6 deals with conditional averaging in the context of large-scale coherent structures, and will address the effects of these features on the SGS dynamics, on the different models, and on how filter scale affects the results. Final conclusions are outlined in §7.

2. Experiment description

2.1. *Facility and instrumentation*

Experiments were performed in the Corrsin Wind Tunnel (Comte-Bellot & Corrsin 1966). The tunnel has a 6×6 m primary inlet with a 25:1 contraction, which feeds into the secondary inlet. Comte-Bellot & Corrsin added a secondary 1.27:1 contraction (to improve isotropy of grid-generated turbulence) which in turn feeds into the 1.2×0.91 m and 10 m long test section. It has the usual gradual increase in the spanwise width along the test section to account for boundary layer growth. A $D = 5.08$ cm diameter smooth cylinder was placed downstream of the secondary contraction. The cylinder diameter was fairly large, with an aspect ratio of only 23 and a blockage of 5.6%, which are not those of an ideal free cylinder wake. A large cylinder was nevertheless

chosen because the emphasis of this study is to use as high a Reynolds number as possible, in order to be able to span a significant range of filter scales in the analysis of subgrid variables. Reproducing precise details of a free wake was not a major goal.

Hot-wire probes were mounted on a Y, Z two-stage stepper motor driven traverse. Translation in the X-direction is manual. Measurements were performed at $x/D = 25$, 50, 75 and 100. Only the vertical portion of the traverse is used in this experiment, which covers 0.48 m of the 0.91 m test section height. This precludes reaching the edges of the wake for the downstream measurement stations. For *in situ* calibration of x-wire probes, a rotation stage was mounted at the end of the traverse arm 0.8 m upstream of the traverse. The rotation stage was originally connected to a stepper motor, but the vibrational loads of the steps imparted to the hot wire were too large, and would invariably break the probe wires. A manual crankshaft using a flexible drive shaft was used instead. An optical encoder with resolution of 0.005° was mounted on the rotation stage so that its angular position would be known.

An Auspex AHWU-100 subminiature single-wire probe was used for well-resolved streamwise velocity (u_1) measurements. An x-wire probe was used to resolve u_1 and u_2 required to simultaneously capture the large-scale coherent structures. The x-wire consists of two of the 12 sensors in a Auspex AVOP-12-100 probe. The original goal had been to resolve the transverse gradients of filtered velocity fields using the 12-wire probe. However, for reasons to be explained later, for the study of subgrid models only streamwise differentiation was ultimately employed since only streamwise filtering is possible (with Taylor's hypothesis). All three probes used 2.5 μm diameter, platinum-plated tungsten wire. The x-wire probes had a length of 0.46 mm while the single wire probe was 0.4 mm in length. The single and x-wire probes were separated by 5 cm in the spanwise direction. The single-wire probe was operated with a DISA 56CT01 constant-temperature anemometer at an overheat ratio of 1.8. The x-wire probes were operated by an A.A. Lab AN-1003 constant-temperature anemometer, at a lower overheat ratio of 1.6 to diminish cross-talk.

For the data set at $x/D = 25$, the calibration was performed at 13 free-stream velocities and nine angles. Using a similar approach as Oster & Wygnanski (1982), the 117 data points were used to least-squares fit a 15-coefficient polynomial, with dependencies on the velocities u_1 and u_2, and the two voltages from the x-wires, E_1, and E_2. Calibration data for the single wire were simultaneously taken while the x-wires were at zero degrees. For $x/D = 25$, this calibration involved seven velocities, whereas at the other measurement stations, only five velocities were used. The polynomial used for the single wire is a modified King's law of the form $u_1 = (D_1E^2 + D_2E + D_3)^2$.

The duration of calibration and data acquisition had to be kept to a minimum because of voltage drift due to probe fouling. Owing to the large thermal mass of the wind tunnel, the short duration prevented keeping its temperature at a constant value during calibration. To correct the voltage readings for temperature changes (which were below 5 °C), a thermocouple was used to record temperature. An additional calibration was performed for temperature dependence, which was repeatably linear and very reliable. For additional details on the experimental setup, calibration, etc. see O'Neil (1996).

After the calibration, the cylinder was placed in the tunnel, and the data were acquired. Sampling rate was 60 kHz, and low-pass filering was performed at 30 kHz. Table 1 contains key parameters of the data sets at each x/D. After the turbulence data were recorded, and the cylinder removed, a second calibration was performed. This was used as a consistency check on the quality of the data. Of all tests reported here, there was no discernible difference in centreline dissipation ε_{CL}, velocity r.m.s.

Two-dimensional cylinder wake	$x/D = 25$	$x/D = 50$	$x/D = 75$	$x/D = 100$
$Re'_D = U_{CL}D/\nu$	7.3×10^4	7.7×10^4	8.9×10^4	8.8×10^4
U_s (m s^{-1})	3.23			
u'_{CL} (m s^{-1})	2.69	1.71	1.50	1.33
ε_{CL} (m^2 s^{-3})	175	37.4	19.3	9.84
R_λ	556	491	516	573
η (mm)	0.065	0.096	0.112	0.133
λ (mm)	3.01	4.17	4.74	6.28
L_1 (m)	0.156	0.140	0.171	0.191
ℓ (cm)	7.44	11.4*	14.2*	16.5*
Skewness	−0.53	−0.51	−0.46	−0.39

TABLE 1. Fundamental quantities of cylinder wake profile data. Values with an asterisk are based on estimated values of U_∞ (see text). For all cases, the sampling rate was 60 kHz, the low-pass filter was 30 kHz for the single-wire and 29.7 kHz for the x-wire probe. There were 2×10^6 points for each probe. All turbulence scales are computed at centreline.

u'_{rms}, or derivative skewness (to within $\pm 0.25\%$). Like most variables of interest in the present study, these quantities depend on changes or derivatives of velocity in the streamwise (temporal) direction, and are thus less sensitive to errors from drift and calibration.

2.2. *Data*

The wake profile was sampled at 15 discrete y-positions, from the centreline to the edge of the wake; 2×10^6 data points were recorded for each of the 15 positions. Four wake profiles were sampled, at $x/D = 25$, 50, 75, and 100. As mentioned before, since the primary interest was to study the subgrid stress and models at high Reynolds numbers, instead of holding U_∞ constant, the largest turbulence Reynolds number was selected at each x/D. Owing to the constraints of the *in situ* calibration, the tunnel speed (measured with a Pitot probe at low x/D but far outside the wake) for measurements at different x/D was set to different values: it was set to the tunnel maximum speed without the cylinder (~ 33 m s^{-1}) minus $3u'_{CL}$, where u'_{CL} is the velocity root-mean-square at the wake centreline of the cylinder. At $x/D = 100$, it was observed in earlier measurements that the edge of the wake came close to the tunnel boundary layers. Thus, the wake properties are expected to deviate from those of a free wake. Since the primary purpose of this data is to study the behaviour of the subgrid stress (SGS) at high Reynolds numbers, and not canonical self-preserving behaviour, this limitation was not considered to be a serious drawback.

Since at the larger downstream distances U_∞ was not measured, the precise defect velocity U_s could not be obtained except at $x/D = 25$ (see table 1). Therefore, r.m.s. data will be normalized with the centreline mean velocity U_{CL} instead of defect velocity. A crude estimate of U_∞ was nevertheless obtained by an extrapolation, which was based on a calibration with compressor speed. This estimate was used solely for purposes of estimating the half-width of the wake ℓ. Table 1 contains the characteristics of each data set.

Additional data were taken at the centreline of the cylinder wake at $x/D = 100$, with the goal of varying the turbulence Reynolds number. For the lowest Reynolds number, a 6.35 mm diameter cylinder was used instead of the 5.08 cm diameter one

$Re'_D = (U_{CL}D)/\nu =$	6.2×10^3	1.8×10^4	4.1×10^4	8.7×10^4
D (mm)	6.35	50.8	50.8	50.8
U_{CL} (m s^{-1})	14.3	5.30	11.8	25.2
u'_{CL} (m s^{-1})	0.57	0.24	0.56	1.17
ε_{CL} (m^2 s^{-3})	13.7	0.094	0.712	8.00
R_λ	89.3	184	377	490
η (mm)	0.123	0.427	0.257	0.140
λ (mm)	2.28	11.4	8.77	5.15
L_1 (m)	0.031	0.109	0.173	0.208
Skewness	−0.37	−0.47	−0.48	−0.38
Sampling rate (kHz)	60	6	20	60
Low-pass filter (kHz)	30	3	10	30

TABLE 2. Fundamental quantities for the wake at $x/D = 100$, on the centreline, for varying Reynolds number.

$Re_M = MU/\nu =$	4.4×10^4	8.9×10^4
Mesh spacing M (cm)	5.08	10.2
x/M	138	69
U (m s^{-1})	12.7	12.8
u' (m s^{-1})	0.13	0.22
ε (m^2 s^{-3})	0.039	0.153
R_λ	85.6	120
η (mm)	0.532	0.377
λ (mm)	9.68	8.13
L_1 (m)	0.083	0.069
Skewness	−0.43	−0.37
Sampling rate (kHz)	10	20
Low-pass filter (kHz)	3	10
Data points/wire ($\times 10^6$)	2	2

TABLE 3. Fundamental quantities of the grid turbulence data.

(see table 2). Grid turbulence at two different Reynolds numbers was also briefly studied. The grids were installed upstream of the secondary contraction. The first grid studied used a 5.08 cm wide mesh, constructed of 0.95 cm thick square bars. The next set used a 10.2 cm wide mesh grid, with 1.91 cm thick square bars. The data characteristics are summarized in table 3.

Throughout this work, Taylor's hypothesis is used to interpret temporal signals as one-dimensional spatial cuts across a three-dimensional turbulent velocity field. The turbulence intensity for the data sets at $x/D = 50$, 75 and 100 was well below 10%, and was 13% for the set at $x/D = 25$. Such levels are believed to be sufficiently low for Taylor's hypothesis to be acceptably accurate, 13% being borderline.

2.3. *Velocity field characteristics*

Before the subgrid stress and models are studied in the next sections, some characteristics of the turbulent velocity field are documented. Figure 1 shows the streamwise and vertical r.m.s. velocities, and the Reynolds stress profiles, normalized with the

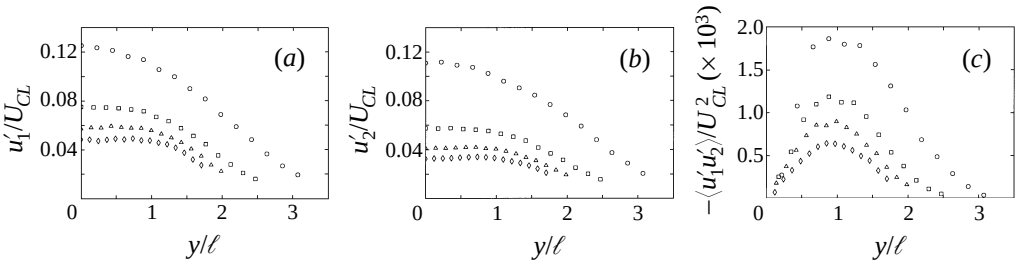

FIGURE 1. Velocity root-mean-square profiles of streamwise u_1 (*a*) transverse velocity u_2 (*b*), and Reynolds shear stress (*c*), at $x/D = 25$ (circles), $x/D = 50$ (squares), $x/D = 75$ (triangles), and $x/D = 100$ (diamonds). Values are normalized with the centreline velocity.

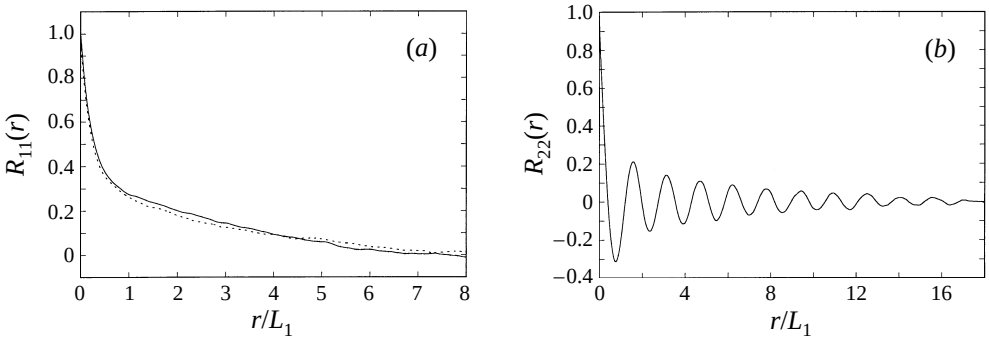

FIGURE 2. (*a*) The longitudinal autocorrelation function of u_1 from the $x/D = 25$ x-wire (solid line) and single-wire (dotted line) data at the centreline (using Taylor's hypothesis). (*b*) The autocorrelation function of u_2, at $x/D = 25$ from the x-wire data. Without using Taylor's hypothesis, the lag between the zero crossings gives the Strouhal frequency. $R_{22}(r)$ at larger x/D are much more similar to (*a*).

centreline mean velocity since the defect velocity is not accurately known. The transverse height is normalized with the half-velocity-defect point, ℓ. At $x/D = 75$ and 100, the rms levels exceed those expected for a fully free wake, probably due to the containing wall effects.

Evaluation of the longitudinal integral scale is based on correlation functions. A typical spatial autocorrelation function of streamwise velocity u_1 is shown in figure 2(*a*), which has been obtained using Taylor's hypothesis at the centreline at $x/D = 25$. Results from both the single and x-wire signals are shown, and agree quite well. The integral scale, L_1, is calculated by numerically integrating $R_{11}(r)$. The u_2 autocorrelation is shown in figure 2(*b*). It displays marked periodicity, arising from the vortex shedding which is still very pronounced at $x/D = 25$, even at this high Reynolds number. This phenomenon will be discussed in more detail in § 6. $R_{22}(r)$ at $x/D \geqslant 50$ no longer shows the sinusoidal behaviour.

Next, viscous-range variables such as molecular dissipation ε are evaluated. However, because of the high Reynolds numbers there is a concern about whether ε could be fully resolved even with the single-wire probe, especially at $x/D = 25$ where the Kolmogorov length is expected to be smallest. A commonly used alternative to measure ε is to use the third-order structure function method valid for locally isotropic turbulence (Monin & Yaglom 1971). When the displacement r falls inside the inertial

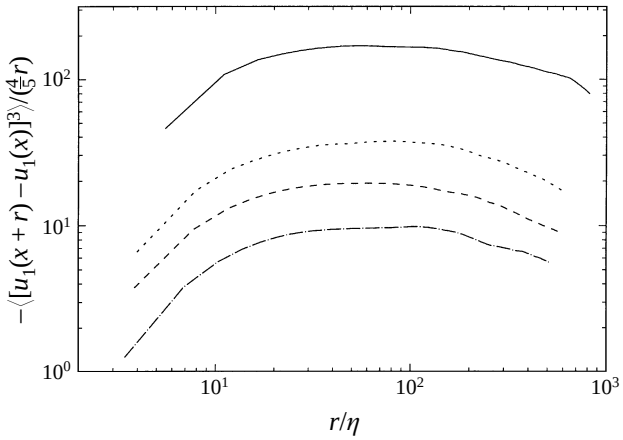

FIGURE 3. Compensated third-order structure functions used to determine ε at the wake centreline (in $m^2\,s^{-3}$). The data are from the single-wire data at $x/D = 25$ (solid line), $x/D = 50$ (dotted line), $x/D = 75$ (dashed line) and $x/D = 100$ (dot-dashes).

range, this allows the dissipation to be obtained according to

$$\varepsilon = -\frac{\left\langle (u_1(x+r) - u_1(x))^3 \right\rangle}{\frac{4}{5}r}. \tag{13}$$

Data from the single wire at the centreline of the four profiles are shown in figure 3. The plateau regions in this figure give the approximate values of ε_{CL}. For instance, for $x/D = 25$, we obtain $\varepsilon_{CL} \simeq 175\,m^2\,s^{-3}$. The other curves also have plateaus inside their inertial ranges, and the respective values of ε_{CL} are listed in table 1. They differed from $15\nu\left\langle (du_1/dx)^2 \right\rangle$, obtained from directly differentiating the signal, by up to about 25% due to above-mentioned lack of resolution at viscous scales and possibly also due to a lack of complete local isotropy.

For reference only, the skewness of the stremwise velocity gradient at the centreline is computed and shown in table 1. These values may also be affected by probe under-resolution of the viscous range. The Taylor microscale and Kolmogorov scale are computed using the estimates of the dissipation, and are shown in table 1.

Figures 4(*a*) and (*b*) show the u_1 spectrum at $x/D = 25$ and $x/D = 100$, respectively. The data are from the single-wire probe. There are several electronic noise spikes at the higher frequencies (caused by the stepper motor driver of the traverse). While the noise spikes have a localized high intensity, they are very narrow and thus their contribution to the variables of interest in this study are negligible, as we have verified. Therefore no effort will be made to remove the noise by additional filtering. The inertial range appears to cover over one decade in length. A $0.55(k_1\eta)^{-5/3}$ line is superimposed (with a one-dimensional Kolmogorov constant of 0.55) giving $C_k = (55/18)(0.55) \approx 1.7$, quite close to the standard value (Monin & Yaglom 1971; Saddoughi & Veeravalli 1994). The u_1 spectra for the cylinder wake at $x/D = 100$ for the five different Reynolds numbers studied, and the data from the grid, are quite similar to figure 4 but, as expected, they fan out differently at low k_1, depending on R_λ.

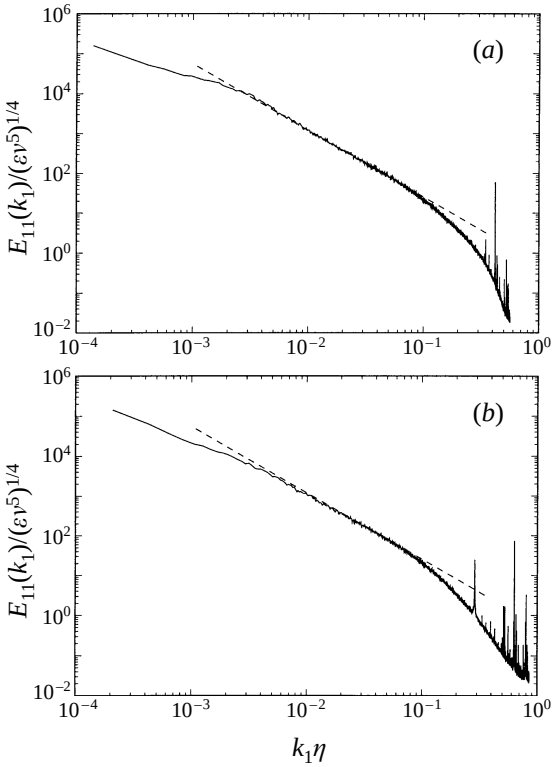

FIGURE 4. Longitudinal spectrum of u_1 at the wake centreline, in Kolmogorov units. Data are from the single-wire probe. A $-5/3$ slope dashed line is superimposed on the inertial range, and gives a one-dimensional Kolmogorov constant of 0.55. (*a*) $x/D = 25$, (*b*) $x/D = 100$.

3. Data analysis and interpretation

The data are analysed by filtering in time, which is interpreted as one-dimensional spatial filtering in the streamwise direction by means of Taylor's frozen flow hypothesis. The filters employed are described in §3.1. In addition to Taylor's hypothesis (*a*), we make two additional key working hypotheses: (*b*) that the subgrid-scale statistics are approximately isotropic, and (*c*) that one-dimensional filtering (as opposed to three-dimensional spatial filtering) introduces effects that can be accounted for, or that they do not qualitatively change the results. These issues are elaborated in §§3.2 and 3.3

3.1. *Filtering*

The analysis of hot-wire data is based upon one-dimensional filtering in the streamwise direction, using Taylor's hypothesis. The resolved velocity $\widetilde{u}_1(x)$ at a scale Δ is computed according to

$$\widetilde{u}_1(x) = \int u_1(x')\, G_\Delta(x - x')\, \mathrm{d}x'. \tag{14}$$

The 1-1 component of the SGS stress tensor is computed according to

$$\tau_{11}(x) = \int u_1(x')\, u_1(x')\, G_\Delta(x - x')\, \mathrm{d}x' - \widetilde{u}_1(x)\widetilde{u}_1(x). \tag{15}$$

For computational convenience, all filtering is done in wave space using the fast Fourier transform (Press *et al.* 1992). Data segments typically consist of 2^{12} points (which is on the order of 10 integral scales). Each segment had its local DC component removed before filtering, and then added back after the filtering operation is complete. Some variables, such as those that enter the dynamic model, involve several successive filtering operations. For the first level of filtering, the overlap-and-save technique (Press *et al.* 1992) is used. For studies that require filtering operations to be performed a second time, periodicity of the data segment is enforced by fully padding the signal with a mirror image of itself (in order to create a periodic signal which is continuous at the edges) before convolving it with the response function. This was found to minimize end effects.

Next, the filters used in this study are described. Most previous *a priori* studies were based on one or more out of three filter types: Gaussian filter, spectral cut-off filter and top-hat (or spatial) box filter (Piomelli *et al.* 1991; Leslie & Quarini 1979). Below, their definitions in one-dimensional are given in wave space.

The cutoff filter eliminates all Fourier modes with wavenumbers above the cutoff wavenumber,

$$G_{\Delta}(k_1) = \begin{cases} 1 & \text{if} \quad k_1 \leqslant \pi/\Delta \\ 0 & \text{otherwise.} \end{cases} \tag{16}$$

It has compact support in wave space, but has a sinc shape $\left(\sin\left(\pi x/\Delta\right) / \left(\pi x/\Delta\right)\right)$ and decays very slowly (as $1/x$) in physical space. It has the conceptual advantage of separating clearly small- and large-wavenumber modes. It has the disadvantage of introducing 'ringing' effects (or Gibbs phenomenon) in physical space when filtering spatially localized phenomena.

The top-hat filter averages the signal in a box of size Δ, and in wave space it becomes

$$G_{\Delta}(k_1) = \frac{\sin\left(\frac{1}{2}k_1\Delta\right)}{\left(\frac{1}{2}k_1\Delta\right)}. \tag{17}$$

Its advantage is a straightforward interpretation in physical space, but in Fourier-space it has a long modulated tail (decaying as $1/k$). This means that 'large' scales also include significant amounts of 'small' scales, and vice versa.

The Gaussian filter is the only filter that has the same shape in physical and wave space, and is defined as

$$G_{\Delta}(k_1) = \exp\left(-\frac{k_1^2\Delta^2}{24}\right). \tag{18}$$

Because it displays a good compromise between spatial and spectral localization, the Gaussian filter will be used in most of this study, unless otherwise noted. Previous investigations (e.g. Meneveau 1994) have found that the impact of using different filter types on the SGS stress, SGS dissipation, model coefficients, etc., is quite small. (The only noticeable exception where filter type has a strong effect is in the correlation coefficient between real stress and the similarity model prediction, where the cutoff filter yields zero correlation while the other filters give a strong correlation (Liu *et al.* 1994). We shall return to this issue in § 6.)

3.2. *Assumption of subgrid isotropy*

As outlined in §1, the variable of most interest in this work is the distribution of SGS energy dissipation $-\langle\tau_{ij}\widetilde{S}_{ij}\rangle$ throughout the wake. From the single-wire measurements, only the 1-1 term (out of a total of six) is available. In analogy with how the viscous

dissipation is estimated from $\partial u_1/\partial x_1$ by assuming small-scale isotropy (see e.g Monin & Yaglom 1971), the SGS dissipation may be estimated by assuming the subgrid scales to be isotropic. We assume that any tensor quantity representing averages of subgrid variables is an isotropic tensor, such as the fourth-rank tensor $\langle \tau_{ij}\tilde{S}_{pq}\rangle$. Its isotropic form is $Q_{ijpq} = \langle \tau_{ij}\tilde{S}_{pq}\rangle = A\delta_{ij}\delta_{pq} + B\delta_{ip}\delta_{jq} + C\delta_{iq}\delta_{jp}$. Using the symmetries $Q_{ijpq} = Q_{jipq}$, $Q_{ijpq} = Q_{ijqp}$, and the divergence-free condition $Q_{ijpp} = 0$, the number of unknown coefficients is reduced from three to one. One obtains

$$Q_{ijpq} = A\left[\delta_{ij}\delta_{pq} - \tfrac{3}{2}(\delta_{ip}\delta_{jq} + \delta_{iq}\delta_{jp})\right]. \tag{19}$$

The term that we measure is Q_{1111}, and from the above $A = -\frac{1}{2}Q_{1111}$. Thus the total dissipation is

$$Q_{ijij} = -\tfrac{1}{2}Q_{1111}\left[\delta_{ij}\delta_{ij} - \tfrac{3}{2}(\delta_{ii}\delta_{jj} + \delta_{ij}\delta_{ji})\right], \tag{20}$$

or

$$\langle \tau_{ij}\tilde{S}_{ij}\rangle = \tfrac{15}{2}\langle \tau_{11}\tilde{S}_{11}\rangle. \tag{21}$$

This shows that under the assumption that SGS motion is isotropic, it is possible to employ the 1-1 component of the tensors only. The term $-\frac{15}{2}\langle \tau_{11}\widetilde{S}_{11}\rangle$, will be called the 'surrogate' SGS energy dissipation. When studying the various models, the same assumption of SGS isotropy will be used.

It is important to stress that the assumption of SGS isotropy may not strictly hold throughout the wake, especially for large filtering scales. Consequently, it will not be possible to interpret spatial variations in surrogate dissipation unequivocally as changes in actual SGS dissipation. Variations in $-\frac{15}{2}\langle \tau_{11}\tilde{S}_{11}\rangle$ could also be caused by changes in SGS anisotropy levels.

3.3. *Effects of filter anisotropy*

As mentioned before, the use of hot wires raises a primary limitation of the experiment, which is that the data can only be filtered in the streamwise direction. Such one-dimensional filtering is substantially different in principle from the usual three-dimensional filtering involved in LES, where all three directions are filtered and coarse grained. Murray, Piomelli & Wallace (1996) have shown using *a priori* tests of DNS in channel flow that considerable discrepancies between three- and one-dimensional (or temporally filtered) variables arise at $y^+ \leqslant 50$, where turbulence structure is strongly anisotropic. For $y^+ \geqslant 50$ the discrepancies were acceptably small.

For isotropic turbulence, Meneveau (1994) has shown that the Smagorinsky coefficient obtained from the 1-1 component using one-dimensional filtering can be simply related to that of three-dimensional filtering using the complete tensor contraction to define the SGS energy dissipation. If C_S^{1D} is the coefficient obtained from one-dimensional filtering and C_S^{3D} is the traditional value, the relationship is

$$C_S^{3D} \approx 1.96 C_S^{1D}, \tag{22}$$

independent of filter size, for Δ in the inertial range. The relationship between the coefficients is independent of Δ because only the 1-1 component of $\widetilde{S}_{ij}$ is used, that is, it only involves derivatives in the filtered streamwise direction. Otherwise, if for instance one were to use one-dimensional filtering in the x-direction, but take derivatives in the (unfiltered) y-direction (e.g. to evaluate $\widetilde{S}_{12}$ using two x-wires displaced along the y-direction), the relationship between C_S^{1D} and C_S^{3D} becomes more complicated and dependent upon Δ (see the analysis by Scotti, Meneveau & Lilly (1993)).

Besides inherent difficulties associated with instrumentation, this is the reason for

not attempting to use derivatives across sensors in the y-direction to (e.g.) construct $\widetilde{S}_{12}$. Since one can only filter in the x-direction, the analysis is limited to taking derivatives in the same x-direction. This leaves the 1-1 components of the tensors to be analysed for purposes of studying the SGS dynamics. When obtaining model coefficients from balancing the rate of SGS dissipation, numerical discrepancies with results from three-dimensional filtering are expected. For the Smagorinsky model, a factor of roughly two is expected (see (22)). For the similarity model, since the filter anisotropy is expected to affect $\langle L_{11}\widetilde{S}_{11}\rangle$ in a similar fashion as $\langle \tau_{11}\widetilde{S}_{11}\rangle$, the discrepancy may be smaller. Overall, the general trends are expected to be robust (e.g. dependence on scale, main features of spatial distributions, etc.).

3.4. *Interpretation of a-priori tests*

In *a priori* tests the model expressions are evaluated based on 'true' velocity fields. However, during a simulation the model may affect the velocity field and give rise to another flow configuration with different statistics. This raises difficulties in interpreting the results of *a priori* tests.

In this study, comparisons between real (surrogate) dissipation and modelled dissipation are made, for which the issue can be stated clearly. Consider, for instance, the Smagorinsky model. In order to predict the correct mean dissipation (which is a necessary condition to reproduce the mean resolved kinetic energy), the expression $C_S^2 2\Delta^2 \langle |\tilde{S}|\tilde{S}_{ij}^2\rangle$ must be 'correct', i.e. it must equal the real dissipation $\langle \tau_{ij}\tilde{S}_{ij}\rangle$. Then the coefficient determined in an *a priori* test is obtained according to (6). In such a test, the 'correct' $\langle |\tilde{S}|\tilde{S}_{ij}^2\rangle$ value is measured from a physically realistic velocity field. A simulation using a different coefficient could still (possibly, but not necessarily) reproduce the correct dissipation by 'adjusting' the value of $\langle |\tilde{S}|\tilde{S}_{ij}^2\rangle$. For instance, if one uses too low a value for C_S, there may be a 'pile-up' of energy near the cutoff scale, and $\langle |\tilde{S}|\tilde{S}_{ij}^2\rangle$ would increase above its 'true' value to attempt to make up for the lower coefficient, and vice versa. However, if this is the case, one already knows that the simulation is doing something wrong to make up for the wrong coefficient.

It may be that the large-scale kinetic energy is still approximately realistic, but a particular statistic of the LES field, typically at small resolved scales, will be unphysical. Depending on applications this may be acceptable, but from a fundamental viewpoint, there is a problem. Thus, the condition that $C_S^2 2\Delta^2 \langle |\tilde{S}|\tilde{S}_{ij}^2\rangle$ be equal to the real dissipation in an *a priori* test is a necessary condition for LES to correctly reproduce the resolved kinetic energy and particular small-scale features of the resolved field (Meneveau 1994). It is from this perspective that the results from the *a priori* tests described in this paper will be interpreted.

4. Mean SGS dissipation and model predictions

4.1. *Real SGS dissipation profiles*

The spatial distribution of the surrogate SGS energy dissipation is computed based on the data according to (21). The results are shown in figure 5(*a–c*) for $\Delta/\eta = 100$, $\Delta/\eta = 50$, and $\Delta/\eta = 20$.

The results are normalized with the viscous dissipation at the centreline (see table 1). The profiles for different downstream locations are seen to agree very well in the inner portion of the wake. The similarity disappears in the outer region, where the dissipation of the near-cylinder stations is seen to decay more slowly away from the centreline. However, not much significance should be attached to this discrepancy

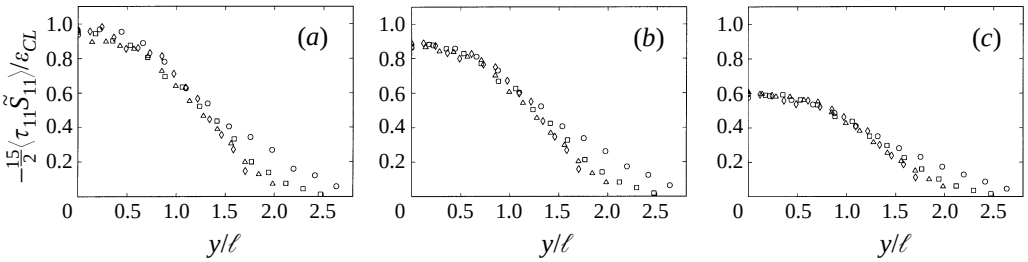

FIGURE 5. Profiles of surrogate SGS dissipation across the wake, at various filter scales. Different symbols correspond to the different downstream locations: $x/D = 25$ (circles), $x/D = 50$ (squares), $x/D = 75$ (triangles), $x/D = 100$ (diamonds). (*a*) $\Delta/\eta = 100$, (*b*) $\Delta/\eta = 50$, and (*c*) $\Delta/\eta = 20$.

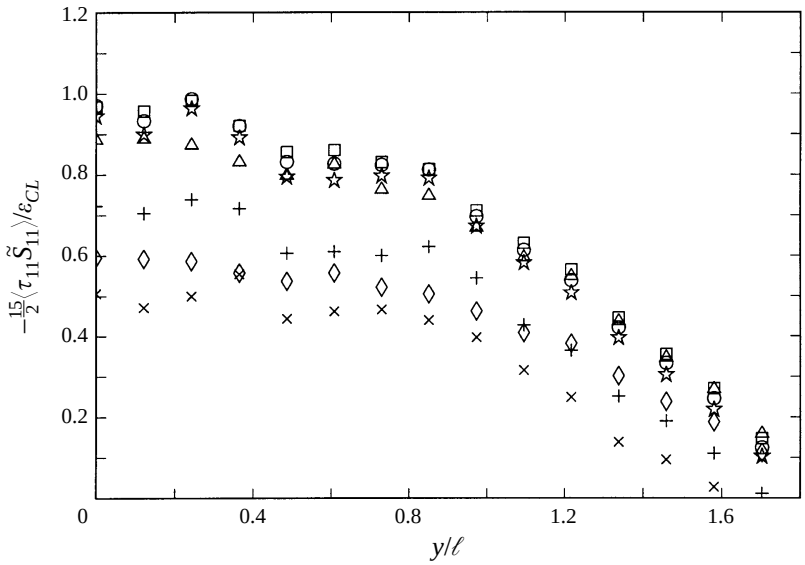

FIGURE 6. Surrogate SGS dissipation profiles across the wake at $x/D = 100$, for different filter lengths: diamonds ($\Delta/\eta = 20$), triangles ($\Delta/\eta = 50$), squares ($\Delta/\eta = 100$), circles ($\Delta/\eta = 150$), stars ($\Delta/\eta = 200$), plus ($\Delta/\eta = 500$) and crosses ($\Delta/\eta = 1000$).

since at the larger x/D, ℓ is estimated rather than directly measured which may affect the scaled results.

In the inertial range, the SGS dissipation is expected to remain independent of filter length, and equal to the molecular dissipation. At $\Delta = 100\eta$, the measured SGS dissipation captures most of ε_{CL}, an indication that at this scale the dynamics are purely inertial. At smaller filter lengths, the observed decrease in SGS dissipation implies that more of the resolved energy is able to be dissipated directly by molecular viscosity.

Next, the dependency of the measured SGS dissipation on filter length, Δ, is examined in more detail for a single downstream distance $x/D = 100$. In figure 6, Δ is varied between 20η and 1000η. As before, the results show that for filter length Δ below 50η more energy is being dissipated directly by viscosity instead of through the SGS scales. Filter levels from $\Delta = 150\eta$ to $\Delta = 1000\eta$ show the opposite trend, in that the SGS dissipation decreases with increasing filter length. At the larger scales, the assumption of isotropy of the subgrid scales can no longer hold. There, the 1-1

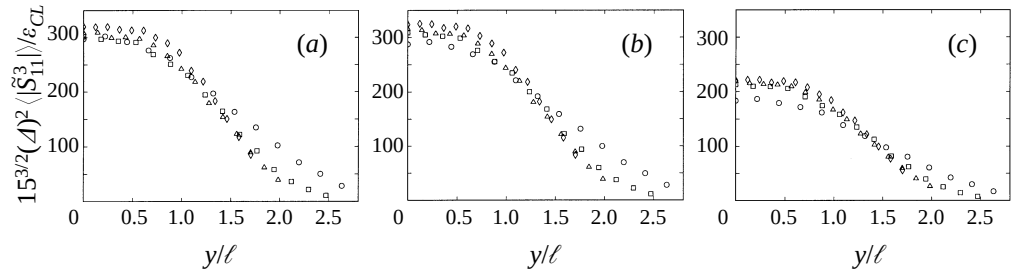

FIGURE 7. Profiles of surrogate SGS dissipation as predicted by the Smagorinsky model form, without multiplying by the Smagorinsky coefficient. Symbols as in figure 5. (*a*) $\Delta/\eta = 100$, (*b*) $\Delta/\eta = 50$, and (*c*) $\Delta/\eta = 20$.

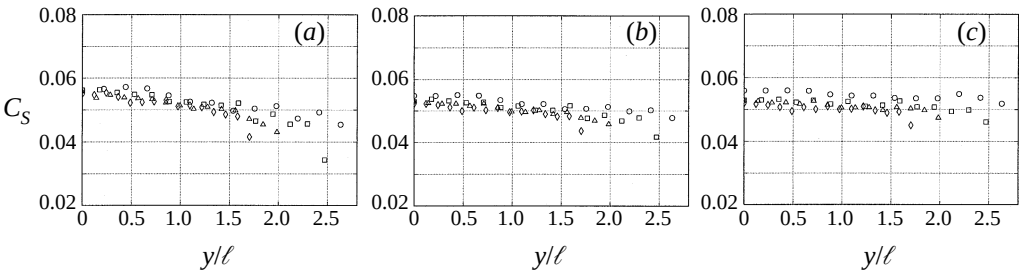

FIGURE 8. Profiles of measured (surrogate) Smagorinsky coefficient across the wake, at various filter scales (symbols as in figure 5). (*a*) $\Delta/\eta = 100$, (*b*) $\Delta/\eta = 50$, and (*c*) $\Delta/\eta = 20$.

component of the strain rate tends to a very small value (in this flow), while the 1-2 component tends (approximately) to the mean of $\partial u_1/\partial y$. It is this term which is responsible for kinetic energy production in the RANS sense. Thus, in the wake the surrogate (1-1) SGS dissipation term does not approach the energy injection rate at large scales, owing to lack of isotropy.

However, the profiles remain quite close in the range of Δ between 50η and 200η. This is indicative of inertial-range behaviour at those scales, and this appears to hold throughout the wake profile. A similar comparison has been performed at different x/D, and the basic trends are found to be unaffected by changes in x/D.

4.2. *Smagorinsky model*

Next, the SGS dissipation provided by the Smagorinsky model is evaluated. By contracting (4) with the resolved strain rate tensor, using the SGS isotropy approximation in (21), and a similar approximation for the strain-rate magnitude for the (smallest) resolved scales, the surrogate Smagorinsky model for the average SGS dissipation becomes

$$(15)^{3/2}\,(\Delta C_S)^2\,\langle|\widetilde{S}_{11}^3|\rangle. \tag{23}$$

The expression $(15)^{3/2}\,\Delta^2\langle|\widetilde{S}_{11}^3|\rangle$, without the coefficient C_S^2 (which will be studied later), is normalized with ε_{CL} and shown in figure 7(*a–c*) for the same three filtering lengths as before. These profiles do not seem to collapse quite as well as $-\frac{15}{2}\langle\tau_{11}\widetilde{S}_{11}\rangle$ did in figures 5(*a–c*), but they follow the same general trends.

The previous measured results may now be substituted into (23), in order to solve

for a measured Smagorinsky coefficient

$$C_S = \left(\frac{-\langle \tau_{11} \widetilde{S}_{11} \rangle}{2\sqrt{15}\widetilde{\Delta}^2 \langle |\widetilde{S}_{11}^3| \rangle} \right)^{1/2}. \tag{24}$$

The results are shown in figure 8(*a–c*) for filter sizes of 100η, 50η and 20η, respectively. One measure of a model's universal applicability is how much or how little the coefficient varies throughout different flow regions and regimes. There are some variations, but in the inner region of the wake, the coefficient is relatively constant. Unlike grid turbulence, the wake contains regions of large mean shear near $y \sim \ell$, especially at $x/D = 25$, and regions of high intermittency in its outer portion. And yet, the observed variations in C_S are weak.

The value obtained at the centreline, $C_S \sim 0.05$–0.06 is quite comparable to the value obtained by Meneveau (1994) for grid turbulence. As mentioned in §3.3, one can relate this value to the coefficient that arises from three-dimensional (instead of one-dimensional) filtering, according to $C_S^{3D} \approx 1.96 C_S^{1D}$, where C_S^{1D} is the measured value (from (24)). This gives $C_S^{3D} \sim 0.1$–0.12, in reasonable agreement with commonly used values in simulations of shear flows (Rogallo & Moin 1984).

Focusing on more detailed features of the results, a mild decreasing trend from the centreline towards the outer edge of the wake can be observed. For $\Delta = 100\eta$, the coefficient ranges from 0.056 at the centreline to ~ 0.04 at the outer edge. The variation is smaller for the smaller filter scale $\Delta = 20\eta$ (figure 8*c*), a trend that is in agreement with the expectation that small scales are more universal than large scales. Nevertheless, the spectra show that even $\Delta = 100\eta$ ($k\eta = \pi\eta/\Delta \sim 3.1 \times 10^{-2}$) is well inside the inertial range (see figure 4). One would therefore expect that the coefficient should be constant there as well. The observed decreasing trend at $\Delta = 100\eta$ means that in the outer regions there is less turbulent energy being cascaded (for a given amount of fluctuating straining motion), than at the centreline. A possible cause for such an effect is outer intermittency, which will be examined in §5.

The agreement between instantaneous values of the measured (1-1) SGS stress and the model is quantified using the correlation coefficient between real and modelled (1-1) component of the stress. The resulting profiles of correlation (not shown) also overlap for different x/D, with peak values of about $\rho \sim 0.3$ near the centreline, and decaying to $\rho \sim 0.1$ near the outer edge of the wake. The correlation coefficient between the measured SGS dissipation and the Smagorinsky model dissipation is also evaluated. Consistent with previous analyses based on DNS (Clark *et al.* 1979), the correlation at the dissipation (scalar) level is larger (near 0.3–0.4) than at the tensor element level.

4.3. *Similarity model*

The similarity model was defined in (7), and is based on the resolved stress L_{ij}. The modelled SGS dissipation accomplished by this model form (without the coefficient c_L) is evaluated from the data by invoking the same isotropy assumptions as before, i.e. we measure $-\frac{15}{2}\langle L_{11}\widetilde{S}_{11}\rangle$. The results are normalized with ε_{CL} and are shown in figure 9. Around the centreline, the profiles collapse less well than those of the real dissipation in figure 5, but better than those of the Smagorinsky model in figure 7.

Using (9), the isotropy assumption, and the data in figures 5 and 9, the similarity

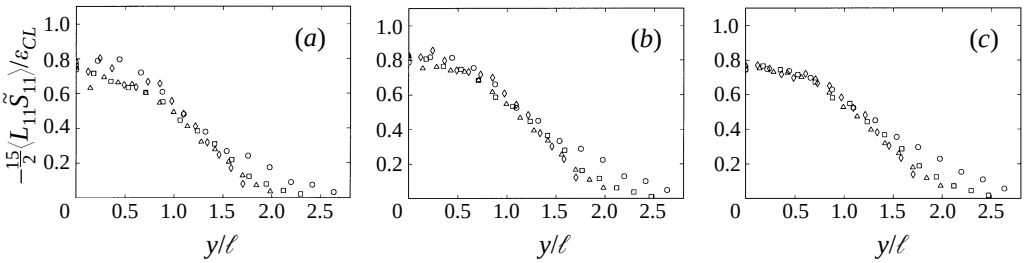

FIGURE 9. Profiles of surrogate SGS dissipation as predicted by the similarity model form, without multiplying by the coefficient C_L. Symbols as in figure 5. (*a*) $\Delta/\eta = 100$, (*b*) $\Delta/\eta = 50$, and (*c*) $\Delta/\eta = 20$.

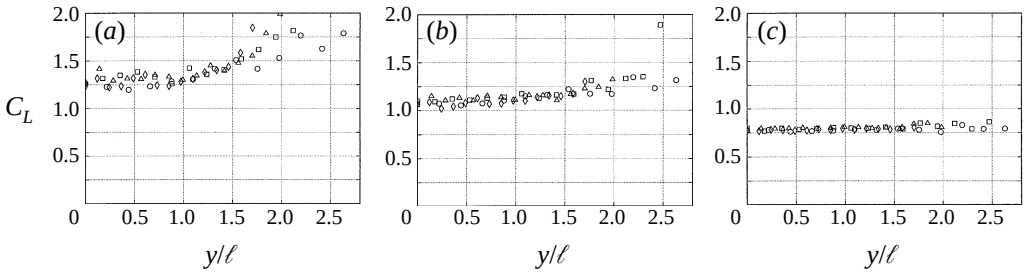

FIGURE 10. Profiles of measured (surrogate) similarity coefficient across the wake, at various filter scales (symbols as in figure 5). (*a*) $\Delta/\eta = 100$, (*b*) $\Delta/\eta = 50$, and (*c*) $\Delta/\eta = 20$.

coefficient is evaluated according to

$$C_L = \frac{\langle \tau_{11}\tilde{S}_{11}\rangle}{\langle L_{11}\tilde{S}_{11}\rangle}. \tag{25}$$

The results are shown in figure 10. As with the Smagorinsky model, a figure of merit of the similarity model is how constant (universal) the coefficient is. At $\Delta = 100\eta$ in figure 10(*a*), the variations of C_L are of similar magnitude as those of C_S in figure 8(*a*), but in the opposite direction, slightly increasing at the wake's outer edge. As can be seen, changes in Δ have considerable impact. For the three filter lengths shown, the change in C_L is $\sim \pm 25\%$, while for C_S it was only $\sim \pm 5\%$. The similarity model, which is based on two filter scales, appears to be more sensitive to scale than the Smagorinsky model. If one of both scales Δ and 2Δ approaches the limits of the inertial range, the coefficient changes.

The value of $C_L \approx 1$ is larger that the value $C_L \sim 0.45$ quoted in Liu *et al.* (1994) for data in the round jet. The reason is that there the similarity model was clipped to eliminate backscatter (it has now become clear that the addition of an eddy-viscosity term, the mixed model, is a better way of eliminating numerical difficulties associated with backscatter). In Liu, Meneveau & Katz (1995), a coefficient of $C_L \sim 1$ (i.e. close to present values) was obtained from the jet data, when no clipping is performed. $C_L \approx 1$ is also consistent with a recent analysis by Cook (1997).

The correlation coefficient between τ_{11} and L_{11} was calculated and was significantly higher (about $\rho \sim 0.75$) than for the Smagorinsky model. This is consistent with the findings of previous investigators (Bardina *et al.* 1980; Liu *et al.* 1994). The correlations observed for the similarity model are higher by about 0.15 than those reported in Liu *et al.* (1994). The latter results were based on coarse-grained

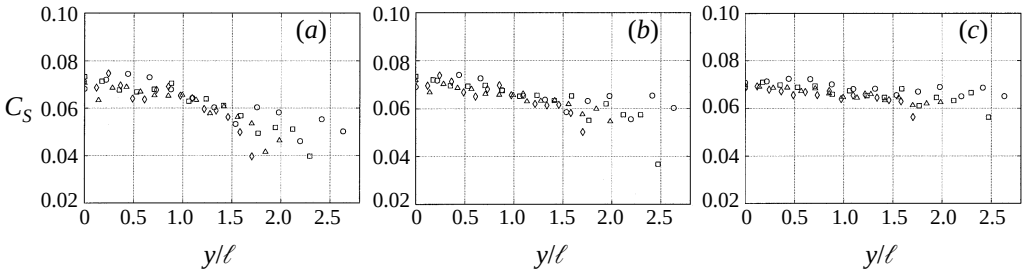

FIGURE 11. Profiles of measured (surrogate) dynamic Smagorinsky coefficient across the wake (symbols as in figure 5). (*a*) $\Delta/\eta = 100$, (*b*) $\Delta/\eta = 50$, and (*c*) $\Delta/\eta = 20$.

data, where L_{ij} was computed from the resolved velocity $\widetilde{\boldsymbol{u}}$, which (in addition to being filtered) had been sampled on a discrete mesh of size Δ. The aim of that approach was to make the comparison based on correlation coefficients more compatible with the coarse-grained information that is available from LES on a discrete mesh. This approach is not followed here, since the focus of the present work is not on correlation coefficients, but on physical field variables such as the SGS dissipation rate (which is usually defined without additional coarse sampling). Finally (as has been observed by others, see e.g. Liu *et al.*), when using the spectral cutoff filter, essentially zero correlation is obtained between τ_{11} and L_{11}. This may be due to the properties of the cutoff filter: when filtering a spatially localized structure, 'ringing' or additional oscillations are generated throughout the domain (Gibbs phenomenon) which causes the correlation among physical-space fields to drop. Additional features of the similarity model with cutoff filtering are studied in § 6.

4.4. *Dynamic model*

The dynamic model was reviewed in §1. To obtain the dynamic Smagorinsky coefficient from the resolved scales of the experimental data, the assumption of isotropy is again invoked. The 'surrogate' of the dynamic coefficient is thus computed according to

$$C_{SD}^2 = \frac{\langle L_{11} M_{11}^* \rangle}{\langle M_{11}^* M_{11}^* \rangle}, \tag{26}$$

where

$$M_{11}^* = -2\sqrt{15}\left((2\Delta)^2 |\widetilde{\widetilde{S}}_{11}| \widetilde{\widetilde{S}}_{11} - \Delta^2 \widetilde{|\widetilde{S}_{11}| \widetilde{S}_{11}}\right). \tag{27}$$

Results are shown in figure 11. The dynamic coefficient is about $\sim 25\%$ higher than C_S in figure 8, but follows similar trends. Here, of course, the coefficient C_{SD} is allowed to vary dynamically, so the variation across the profile or with a change in Δ is not a problem *per se*. It is encouraging that the coefficient displays a similar decay toward the outermost part of the wake as the real coefficient C_S, although the trend is slightly more pronounced. While C_S is based on third-order moments, C_{SD} is based on fourth-order moments, with statistical convergence less satisfactory as evidenced by the increased scatter. Given the many approximations used in measuring C_{SD}, the observed 25% difference in magnitude with C_S cannot be attributed much significance at this stage.

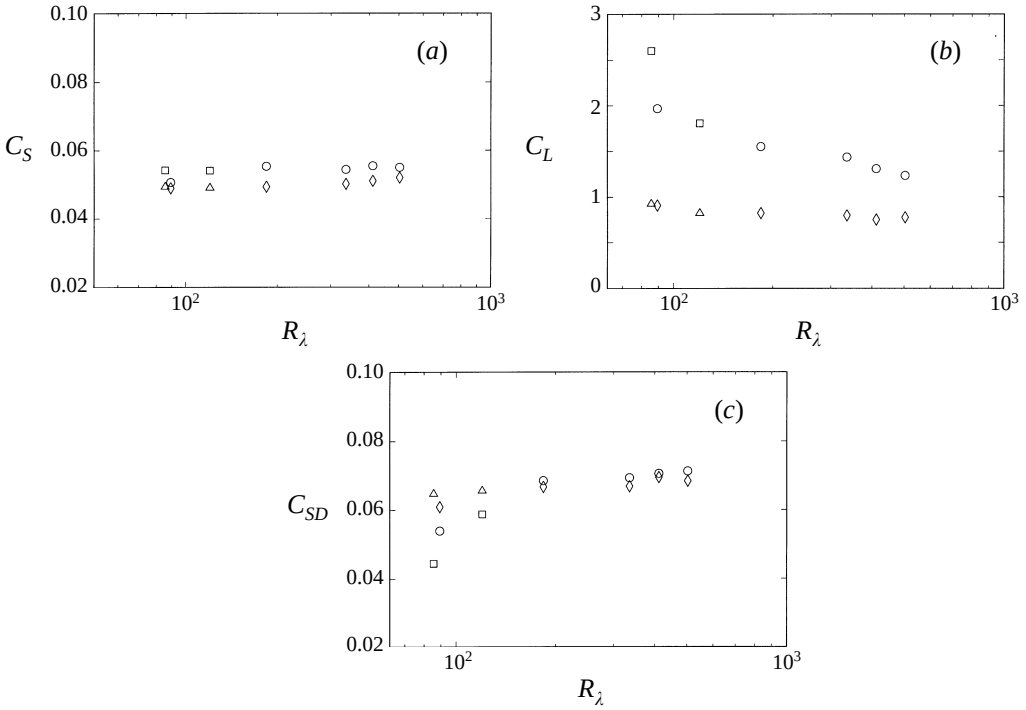

FIGURE 12. (*a*) Surrogate Smagorinsky coefficient, (*b*) surrogate similarity coefficient and (*c*) surrogate dynamic Smagorinsky coefficient as a function of R_λ, at the wake centreline (circles: $\Delta/\eta = 100$, and diamonds: $\Delta/\eta = 20$) at $x/D = 100$; and in grid turbulence (squares: $\Delta/\eta = 100$ and triangles: $\Delta/\eta = 20$).

4.5. *Reynolds number dependence*

In this section the effect of Reynolds number on model coefficients is documented. Data from the grid and cylinder at the centreline, described in tables 3 and 2, are analysed with $\Delta = 20\eta$ and 100η (Gaussian filter). The Smagorinsky coefficient is shown in figure 12(*a*), and for both flows shows essentially no sensitivity to R_λ, and only a weak dependence on scale. The similarity coefficient in 12(*b*) shows little dependence on R_λ at $\Delta/\eta = 20$, but for $\Delta = 100\eta$ it varies considerably. It should be noted that the filter is held constant, and especially for the lower values of $R_\lambda = 86$, $2\Delta = 200\eta$ is already larger or comparable to the integral scale.

In regard to the dynamic Smagorinsky model, C_{SD} in figure 12(*c*) shows similar behaviour to C_S for $R_\lambda \geqslant 184$, but shows a decrease at lower Reynolds numbers for the larger filter size $\Delta/\eta = 100$. Like C_L, C_{SD} is based on a test-filter scale of $2\Delta = 200\eta$ which already falls outside the expected scaling range. Yet C_{SD} appears to be less variable at lower Reynolds numbers than C_L.

The results confirm that as long as all relevant filter scales are well inside the inertial range, there is no appreciable Reynolds number effect on coefficients. The similarity model appears to be more sensitive to approaching the scaling limits than the Smagorinsky model.

5. Effects of outer intermittency on the Smagorinsky coefficient

The decay of C_S across the profile, observed in §4.2 for a significant part of the inertial range, means that the Smagorinsky model with a uniform coefficient appropriate to the wake centreline provides excessive damping near the wake's edges. This situation is reminiscent of the excessive mixing provided by the classical mixing length closure in the RANS approach (Tennekes & Lumley 1972). In the outer parts of the wake, it has been argued (Tennekes & Lumley 1972) that outer intermittency (Corrsin 1943, 1955; Townsend 1956) may decrease the effective turbulent mixing, due to the presence of significant portions of irrotational flow.

A similar effect may be at play for SGS motions: the real SGS dissipation is associated with true turbulent motion and should, arguably, be small in the irrotational portions of the flow. On the other hand, the mean dissipation from the Smagorinsky model may contain contributions from irrotational strains, and may thus overestimate SGS dissipation. In order to ascertain if this is the reason for the slight decreasing trend observed previously in C_S (see figure 8), an attempt is made to discriminate among turbulent and non-turbulent events using conditional averaging. At issue is whether C_S computed only within the turbulent regions (i.e. eliminating the effect of irrotational flow) varies less than the global value.

To this end, an indicator function $I(x)$ with the property that $I(x) = 1$ if $x \in$ turbulent region and $I(x) = 0$ if $x \in$ non-turbulent region is constructed. With $I(x)$, one may define an intermittency function Γ according to

$$\Gamma = \langle I \rangle = \lim_{L_0 \to \infty} \frac{1}{L_0} \int_0^{L_0} I(x)\,\mathrm{d}x. \tag{28}$$

If the flow is completely turbulent, $\Gamma = 1$, while if it is always non-turbulent, $\Gamma = 0$. The subscripts T and N will be used to denote turbulent and non-turbulent conditional averages, respectively. The first conditional moments of any arbitrary variable Q then become

$$\langle Q \rangle_T = \langle Q(x)\,|I(x) = 1\rangle = \lim_{L_0 \to \infty} \frac{1}{\Gamma L_0} \int_0^{L_0} Q(x) I(x)\,\mathrm{d}x, \tag{29}$$

and

$$\langle Q \rangle_N = \langle Q(x)\,|I(x) = 0\rangle = \lim_{L_0 \to \infty} \frac{1}{(1-\Gamma) L_0} \int_0^{L_0} Q(x)\,(1 - I(x))\,\mathrm{d}x. \tag{30}$$

The first unconditional moment is

$$\langle Q \rangle = \Gamma \langle Q \rangle_T + (1 - \Gamma)\,\langle Q \rangle_N. \tag{31}$$

We will measure the conditional real and modelled SGS dissipation in both turbulent and non-turbulent regions, and derive the corresponding conditional Smagorinsky coefficient. The Smagorinsky coefficient corresponding to the turbulent region is obtained according to

$$C_S^2\big|_T = -\frac{\langle \tau_{11} \widetilde{S}_{11} \rangle_T}{2\sqrt{15}\widetilde{\Delta}^2 \langle |\widetilde{S}_{11}^3| \rangle_T}. \tag{32}$$

5.1. *Indicator function*

A number of papers have examined the phenomenon of outer intermittency and documented inherent difficulties in discriminating between 'turbulent' and 'non-turbulent' portions of the flow based on hot-wire data (Corrsin 1955; Kovasznay, Kibens &

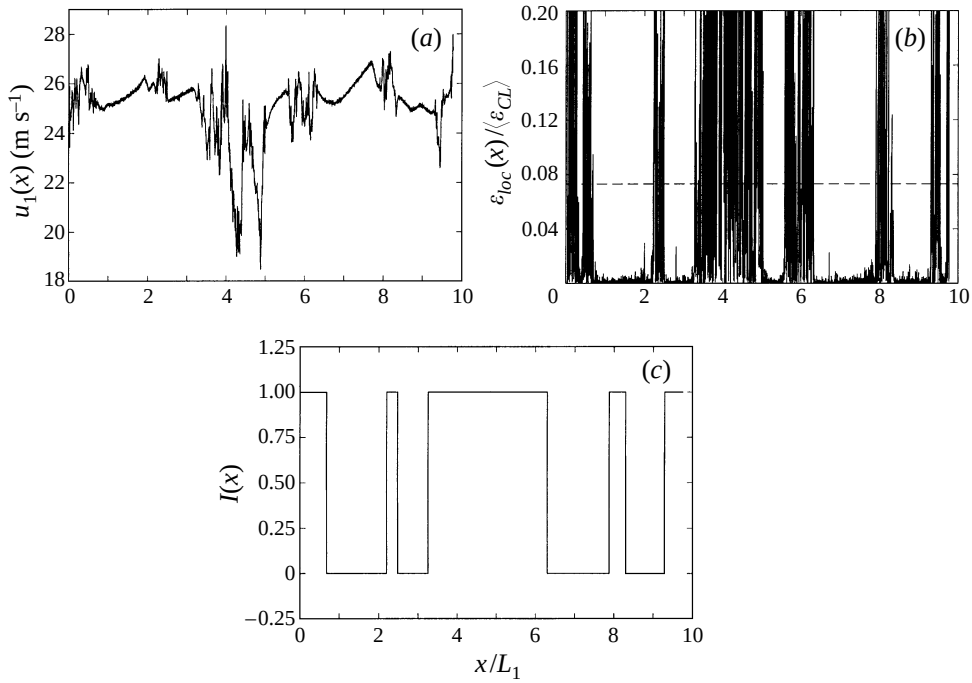

FIGURE 13. A sample of signals illustrating the process of constructing the indicator function, at a cross-stream distance of $y/\ell = 1.97$ (at $x/D = 25$). (*a*) The streamwise velocity, $u_1(x)$. (*b*) The local (pseudo) dissipation, $\varepsilon_{loc}(x)$ compared with the threshold level. (*c*) The resulting indicator function, after applying the hold-length criterion.

Blackwelder 1970; Kollman 1982; Chen & Blackwelder 1978; Antonia & Atkinson 1974). Hedley & Keffer (1974) and Muck (1980) have studied fundamental questions concerning discrimination and the dependence of conditional moments on threshold levels. For present purposes, one of the simpler approaches will be used, consisting of five steps that will be explained below in detail: smoothing of the data, establishing a detector function, setting a threshold on this function, using the results to construct an indicator function, and lastly, applying a hold length. Figure 13(*a–c*) illustrates the approach based on a segment of the data.

First, and only for the purpose of constructing the indicator function, the velocity is low-pass filtered at a scale 15η to eliminate unwanted noise. The focus of this study is on SGS modelling with filtering at a much larger scale of $\Delta = 100\eta$, which should mitigate any potential overlap in scale with the detector function.

Next, a variable is chosen which should ideally be representative of turbulence, the 'detector function' (Murliss and Bradshaw 1974). We employ the local dissipation calculated according to $\varepsilon_{loc} = 15\nu(\partial u_1/\partial x)^2$ and normalized with the average dissipation on the centreline.

Once the detector function is chosen, a threshold level must be selected which must be well above the maximum amplitude level of background noise. The threshold selected in our example is $\varepsilon_{thres} = 0.073\varepsilon_{CL}$ (where ε_{CL} is the mean dissipation at the centreline), and is shown in figure 13(*b*) as a dashed line. While there are noise spikes below the threshold, the spikes above the threshold are clearly due to turbulence and not to noise. To verify this, data were taken without the cylinder present, at several

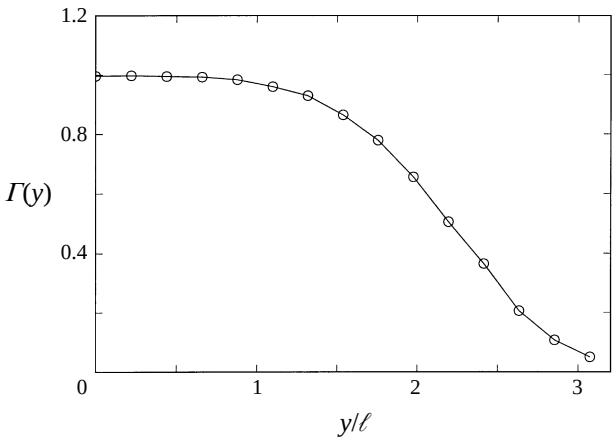

FIGURE 14. Profile of intermittency function $\Gamma(y)$.

y-values in the same manner as with the cylinder. The same procedure was used to verify that the signal exhibited no spikes above the selected threshold level.

A preliminary indicator function, $I^*(x)$, can then be locally turned on whenever the detector function is greater than the threshold level. However, it is possible to get spurious, short, dropouts ($I^* = 0$) because of high-wavenumber (inner) intermittency. The traditional approach to account for this effect has been to utilize a hold length, ξ_H. Spurious dropouts are reduced by imposing that anytime a turbulent event contains a non-turbulent event with a pulse-width length that is less than the hold length, the non-turbulent event is 'filled' in and treated as a turbulent event. The hold length used is $\xi_H = 0.56L_1$ or equivalently $\xi_H = 1.3 \times 10^3\eta$, where L_1 and η are the integral and Kolmogorov scales at the wake centreline. As seen in figure 13(b), near $x/L_1 \approx 0.3$ there are two nearby events that have been identified as turbulent, whose separation is less than ξ_H. The lull is thus 'filled' in and only one block of turbulence is left. While reducing spurious dropouts, a risk is taken that a non-turbulent fluid parcel would be falsely included as a turbulent event. This has probably occurred near $x/L_1 \approx 5.2$. The effect of using different hold lengths, thresholds, and detector functions have been explored in detail (O'Neil 1996), but details will not be repeated here.

Using the parameters introduced before (dissipation as the detector function, threshold $\varepsilon \geqslant 0.073\varepsilon_{CL}$, $\xi_H = 0.56L_1$) the indicator function $I(x)$ is constructed for the entire data at $x/D = 25$. Figure 14 shows the resulting profile of the intermittency function, $\Gamma(y) = \langle I \rangle$, across the wake. With the indicator function, the conditionally averaged subgrid dissipation rates may now be computed also.

5.2. *Results*

The surrogate SGS dissipation is computed at $\Delta = 100\eta$ and is conditionally averaged. Figure 15(a) shows profiles of $-\langle \tau_{11}\widetilde{S}_{11}\rangle_T$ and $-\langle \tau_{11}\widetilde{S}_{11}\rangle_N$ compared to the unconditional moment $-\langle \tau_{11}\widetilde{S}_{11}\rangle$ across the wake. Near the centreline, $\langle \tau_{11}\widetilde{S}_{11}\rangle_T \approx \langle \tau_{11}\widetilde{S}_{11}\rangle$. As one moves towards the edge, the unconditional subgrid dissipation decays at a faster rate than the SGS dissipation conditioned on turbulent events. This is expected since the unconditional moment contains a significantly larger percentage of non-turbulent events near the wake edge.

Figure 15(b) shows profiles of $\langle |\widetilde{S}_{11}|^3\rangle_T$ and $\langle |\widetilde{S}_{11}|^3\rangle_N$ compared to $\langle |\widetilde{S}_{11}|^3\rangle$. The conditional and unconditional averages display similar trends as figure 15(a), for the

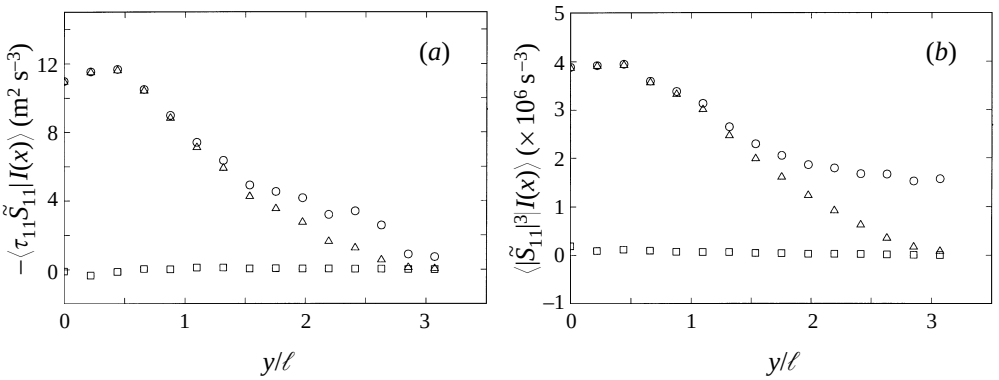

FIGURE 15. (*a*) The conditional subgrid dissipation for both turbulent and non-turbulent events. (*b*) The conditional resolved cubed strain rate magnitude for both turbulent and non-turbulent events. Triangles: unconditional moments, squares: non-turbulent averages ($I = 0$), circles: turbulent averages ($I = 1$).

same reasons. However, the turbulent average decays less strongly at the edge than in figure 15(*a*). This suggests that the Smagorinsky coefficient in the turbulent regions again decays, at the outer portions of the wake.

Most noticeable is the negligible values of the non-turbulent averages compared to the turbulent ones. The modelled SGS dissipation which was argued to possibly contain contributions from the outer non-turbulent fluctuating strain is negligible in the non-turbulent regions of the signal. The implications for the Smagorinsky coefficient are immediate, since one can write

$$\langle \tau_{11}\widetilde{S_{11}}\rangle = \Gamma \langle \tau_{11}\widetilde{S_{11}}\rangle_T + (1-\Gamma)\langle \tau_{11}\widetilde{S_{11}}\rangle_N, \tag{33}$$

and neglecting the non-turbulent part one obtains $\langle \tau_{11}\widetilde{S_{11}}\rangle \approx \Gamma \langle \tau_{11}\widetilde{S_{11}}\rangle_T$.

Given the results of figure 17(*b*), a similar approximation is warranted for the Smagorinsky term, $\langle |\widetilde{S}|^3 \rangle \approx \Gamma \langle |\widetilde{S}|^3 \rangle_T$. Replacing in (32) yields that the Smagorinsky coefficient valid inside the turbulent region is approximately equal to the unconditional value, i.e. $C_S|_T \approx C_S$.

Therefore, conditional averaging based on outer intermittency does not yield a more constant model coefficient across the wake. A number of sensitivity studies were done (O'Neil 1996) and it was found that this conclusion is quite robust with regard to the various parameters that entered the construction of the indicator function.

6. Coherent structures and phase-averaging

In §4, the relationship between SGS dissipation and the mean velocity field of the wake was explored. This was followed by an analysis of the effect of outer intermittency on the Smagorinsky coefficient, with little dependency found. Another feature of the flow field which is ubiquitous in turbulent shear flows is the presence of large-scale coherent structures (Brown & Roshko 1974; Crow & Champagne 1971). Townsend (1956) used measurements of the velocity autocorrelation function in a cylinder wake to infer the presence of large quasi-deterministic eddies on top of the turbulent scale range. Cantwell (1981) credits him with being the first to draw a concrete picture of organized large-eddy motion and to realize its importance in

controlling turbulent transport. Probably one of the most pronounced features of the cylinder wake is the initial formation of organized alternating two-dimensional vortices, the Kármán vortex street. Cantwell & Coles (1983), Hussain & Hayakawa (1987, hereafter denoted HH) and Matsumura & Antonia (1993) have extensively studied such wake structures from the point of view of phase-decomposed Reynolds averaging, entrainment and transport.

LES has the advantage that such structures are (typically) resolved in the simulation, and need not be modelled. A question that has not been addressed before in the context of the plane turbulent wake is what effect coherent structures have on features of the SGS dynamics such as SGS dissipation of kinetic energy. If there is an effect, one wonders how this is represented by the various models. In this section, we employ conditional averaging with respect to coherent structures in the wake to study the conditional SGS dissipation and the model predictions.

6.1. *Eduction via phase averaging*

Roshko (1954) showed that clearly defined periodicity of the Kármán vortex street seemed to disappear at about $x/D = 50$. Therefore, like the intermittency study in §5, attention will remain focused solely on the data at $x/D = 25$. As can be seen from figure 4, there is no peak evident at any wavenumber (frequency) for the streamwise velocity component. Spectra of vertical velocity, u_2, show a dominant and compact peak at the Strouhal frequency. The peak frequency is $f_S = 87.9$ Hz, giving Strouhal number $S_t = 0.181$. For reference, Cantwell & Coles' (1983) data were at $Re_D = 1.4 \times 10^5$, $x/D = 1$–8, and they found $S_t = 0.171$. HH sampled at $Re_D = 1.3 \times 10^4$, $x/D = 10$, 20 and 40, and found $S_t = 0.21$. The Strouhal mode and its neighbouring component on each side contain 20% of the total u_2-variance. The amount of energy density at f_S is over ten times greater than in the neighbouring incoherent large-scale turbulence. Spectra at other y/ℓ also displayed a similar peak, but of decreasing magnitude as y/ℓ increases.

The ubiquity of the Strouhal peak at all y/ℓ locations allows us to use phase averaging to identify coherent structures. Moreover, the results of HH (who used a vertical array of probes for simultaneous measurements across y) clearly show that the conditional iso-u_2 contours are vertically oriented, that is to say the iso-u_2 structures are not inclined. This implies that the phases of the sinusoidal component of u_2 at f_S are about the same at all y-locations. This in turn means that one may use independent measurements at different y-locations by traversing a single probe, and synchronizing the phases of the band-pass filtered u_2 signal during post-processing. This is the approach followed by Matsumura & Antonia (1993).

To minimize problems with spectral resolution of f_S, long segment sizes should be used to perform the notch filtering in a narrow band around $f_S = 87.9$ Hz. On the other hand, using very long segments has the disadvantage that phase-jitter in the full signal is not accounted for. As a good compromise between these competing requirements (see O'Neil 1996 for more details), a segment size of 2^{13} points (a length of 0.136 s) is used, containing 11–12 periods of the Strouhal signal. The local phase ($\Phi = 0$) is defined for each segment by the first upward zero crossing of the notch-filtered u_2 detector signal. No attempt is made to extrapolate outside the first and last zero crossing of each 2^{13} segment, since the amount of trimmed data is small. Phase-averaged variables are evaluated by discretizing the phase $\Phi \in (0, 2\pi)$ into m bins and conditionally averaging variables for each bin.

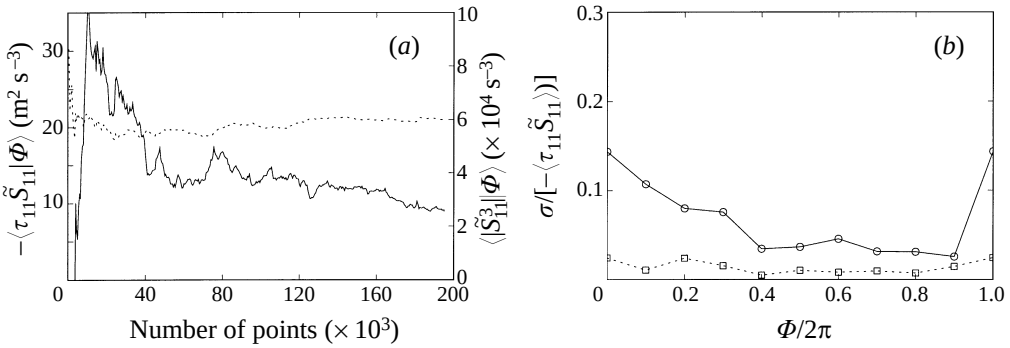

FIGURE 16. (*a*) Convergence history (running averages) of $-\langle \tau_{11}\widetilde{S}_{11}|\Phi\rangle$ (solid line, left-hand scale) and $\langle |\widetilde{S}_{11}|^3|\Phi\rangle$ (dotted line, right-scale), in dimensional form. Data are at the centreline, at $\Delta = 200\eta$. There were $m = 10$ bins used for the conditional averaging. (*b*) Root-mean-square of the last half of the convergence history, normalized by the actual or modelled SGS dissipation.

6.2. *Statistical convergence*

The next concern is with statistical convergence of small-scale variables measured with the single-wire probe. In earlier sections, all 2×10^6 points at each location were available for averaging. Now, only a fraction $1/m$ of the data is available at each phase. One possible estimate for the convergence uncertainty is to evaluate 'running conditional averages' using from a few to the total of $2 \times 10^6\,\mathrm{m}^{-1}$ points to compute the averages. Figure 16(*a*) shows running averages of both the real and Smagorinsky dissipation at a certain phase ($\Phi = 0$), from data obtained at the centreline, with a filter of $\Delta/\eta = 200$. The discretization uses $m = 10$, meaning that 10^5 points are available in each bin. Clearly the Smagorinsky term converges significantly better than the real SGS dissipation. It is well known that convergence of turbulence odd-order moments (such as $\langle \tau_{11}\widetilde{S}_{11}\rangle$) is more difficult to achieve than for even-order (or the absolute values of odd-order) moments. The degree to which such variables attain their asymptotic value may be quantified by evaluating the r.m.s. of the running averages over the last half of the data, that is, using from $10^6\,\mathrm{m}^{-1}$ to $2 \times 10^6\,\mathrm{m}^{-1}$ points. Figure 16(*b*) plots this r.m.s. for the phase-averaged SGS and Smagorinsky dissipations. The values are normalized with the respective mean SGS dissipation averaged over all 2×10^6 points without phase averaging. While $\langle |\widetilde{S}_{11}^3||\Phi\rangle$ does relatively well (with σ typically below 3%) at all phases, the actual SGS dissipation has larger errors (with σ between 5% and 15%). The worst convergence is for the bin at $\Phi = 0$, for which the running averages are shown in (*a*). The other bins display better convergence histories. Similar results were obtained by using $m = 20$ and $m = 30$. The main focus of the analysis of phase-averaged distributions will be qualitative, for which the present convergence accuracy is deemed acceptable.

From here on, phase-averaged variables will be denoted by $\langle \dots \rangle_c$, and the explicit reference to phase Φ will be omitted for convenience.

6.3. *Construction of pseudo-two-dimensional contours*

Data at each y/ℓ are phase discretized into $m = 20$ bins. The velocities are expressed in a coordinate system convecting with the rollers at a speed U_c, defined as the mean velocity at the y/ℓ location at which the peak vorticity is observed (see below). To enhance visual clarity, the data are extended in both the y- and the (pseudo) streamwise direction. Periodicity is employed to plot a total range of phase equal to

4π. Furthermore, the data are extended in the $-y$-direction by assuming symmetry and phase reversal about the centreline (since measurements were only performed on one side of the wake). Adding an additional bin at $\Phi = 4\pi$ (equal to the values at $\Phi = 0$), the total data matrix is then 41×29. To reduce jitter in the contours, a moving two-dimensional average is applied to the fields, over the four neighbouring bins (2 in each direction). The data matrix is thus reduced to 40×28 bins.

6.4. *Coherent velocity field*

Figure 17 shows results pertaining to the phase-averaged velocity field. The $\langle u_1 \rangle_c$ and $\langle u_2 \rangle_c$ components from the x-wires are plotted as velocity vectors. Note that only one-quarter of the figure is measured, the other three quadrants being obtained as outlined in the preceding section. The $\langle u_1 \rangle_c$ component is reduced by $U_c = 22.54\,\mathrm{m\,s^{-1}}$, since the frame is moving at U_c in the streamwise direction. The flow is from left to right. There are three roll centres on the top, and two on the bottom. Conversely, there are two saddle points above the centreline, and three below it. The agreement between this phase-averaged vector field with the educed fields from HH is good, even though some differences in the eduction method exist and the present Reynolds number is higher. The vertical extent of the figures corresponds to 6.2ℓ. The horizontal extent is $2 \times U_c/f_S = 6.9\ell$ (using Taylor's hypothesis with the roller convection velocity).

The coherent spanwise vorticity is defined as

$$\langle \omega_3 \rangle_c \equiv \frac{\partial \langle u_2 \rangle_c}{\partial x} - \frac{\partial \langle u_1 \rangle_c}{\partial y}, \tag{34}$$

and is evaluated from the phase-averaged velocities. The vorticity is then normalized by the wake half-velocity-defect height and wake deficit velocity, $U_s = 3.23\,\mathrm{m\,s^{-1}}$. The minimum and maximum scaled vorticity is ± 1.36, and is located at the roll centres, $y_c/\ell = \pm 0.88$. This gives the location at which $U_c = \langle u_1(y_c) \rangle$ is obtained. Figure 17(*a*) shows the conditional spanwise vorticity contours. The vectors are superimposed on the vorticity contours as an aid in locating the critical points and structure in the field. The contours are given at ten discrete evenly spaced levels between the minimum and maximum values. There seems to be good spatial agreement with the contours from HH. They measured a peak vorticity magnitude of $\langle \omega_3 \rangle_c / S_m = 6$, where $S_m D/U_\infty = 0.105$ was the maximum mean shear. The maximum mean shear for this experiment is $S_m D/U_\infty = 0.0611$, so that the maximum strength of the vorticity field is $\langle \omega_3 \rangle_c / S_m = 1.90$. This discrepancy is probably due to the differences in eduction scheme. The vortices of HH are stronger, since unlike the phase-averaging used here, HH only kept about 13% of the data, rejecting the rest as non-coherent events.

Contours of $\langle S_{11} \rangle_c = \langle \partial u_1/\partial x \rangle_c$ are shown in figure 17(*b*). The coherent strain $\langle S_{12} \rangle_c$ is evaluated according to

$$\langle S_{12} \rangle_c = \frac{1}{2}\left(\frac{\partial \langle u_1 \rangle_c}{\partial y} + \frac{\partial \langle u_2 \rangle_c}{\partial x} \right). \tag{35}$$

Contours are shown in figure 17(*c*), and are substantially stronger than $\langle S_{11} \rangle_c$. Maxima are located at the saddles, and $\langle S_{12} \rangle_c$ is very weak at the roll centres.

The incoherent Reynolds shear stress $-\langle u_1' u_2' \rangle_c$ (where $u_i' = u_i - \langle u_1 \rangle_c$) is shown in figure 17(*d*). Again, data from the x-wires have been employed. Extrema are at the saddle points, and contours are slightly inclined along the separatrix. This agrees rather well with the results of HH. If $-\langle u_1' u_2' \rangle_c$ is normalized with U_∞^2 instead, the

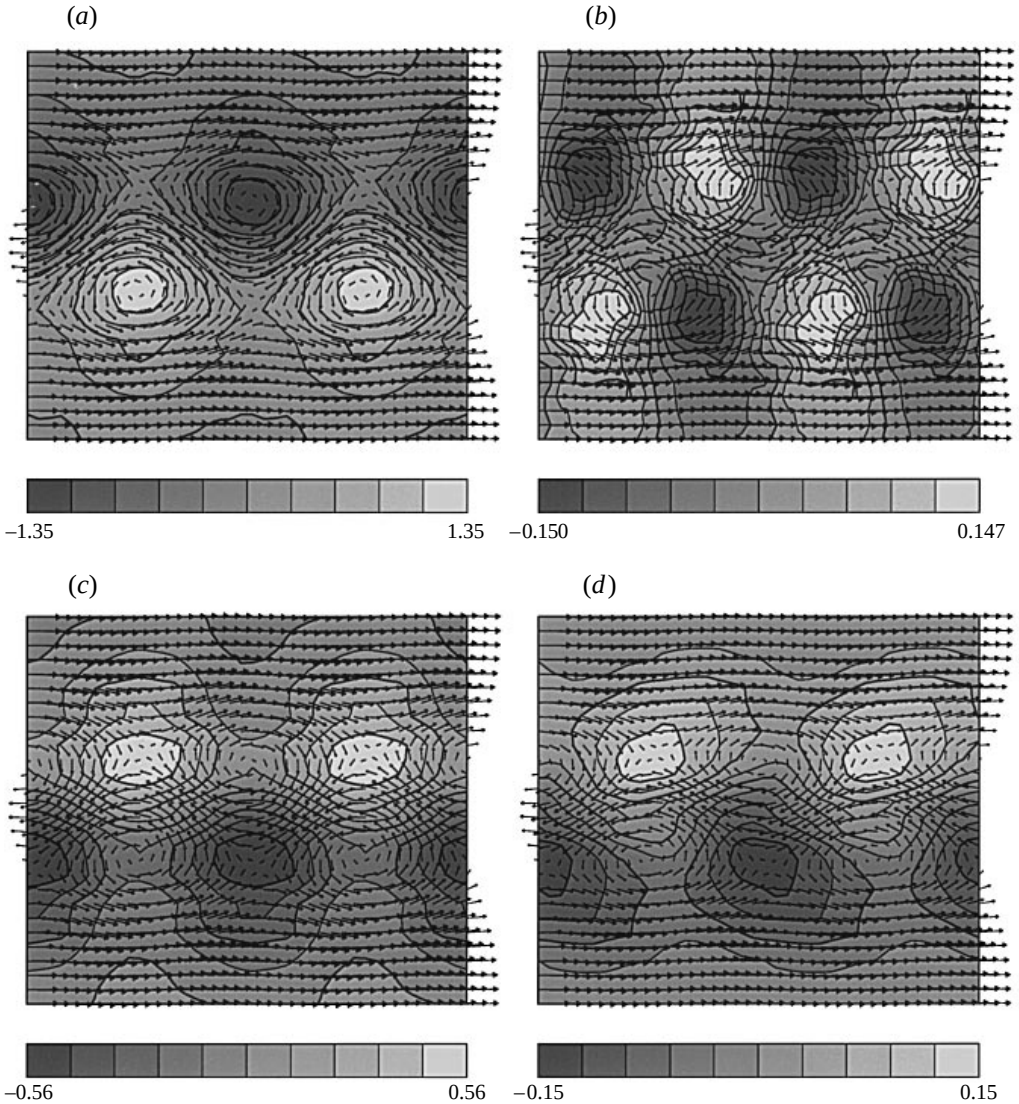

FIGURE 17. Vectors: conditionally averaged velocity field in a frame moving with the rolls, in the intermediate wake of a cylinder at $x/D = 25$. Velocity magnitude of arrows at corners is 2.24 m s^{-1}. Contours in (*a*) correspond to the phase-averaged spanwise vorticity $\langle \omega_3 \rangle_c / (U_s/\ell)$, (*b*) contours of $\langle \widetilde{S}_{11} \rangle_c / (U_s/\ell)$, (*c*) contours of $\langle \widetilde{S}_{12} \rangle_c / (U_s/\ell)$, (*d*) contours of incoherent Reynolds shear stress $-\langle u_1' u_2' \rangle_c / U_s^2$.

incoherent Reynolds stress intensity levels become ± 0.24, as compared to the HH results of ± 0.5. Also, some discrepancies with the incoherent normal Reynolds stresses of HH were observed. Again, discrepancies are due most probably to the less stringent eduction scheme used here.

These results show that phase averaging applied to the current data set at $x/D = 25$ yields expected behaviour in terms of the coherent fields, and important incoherent variables such as Reynolds shear stress.

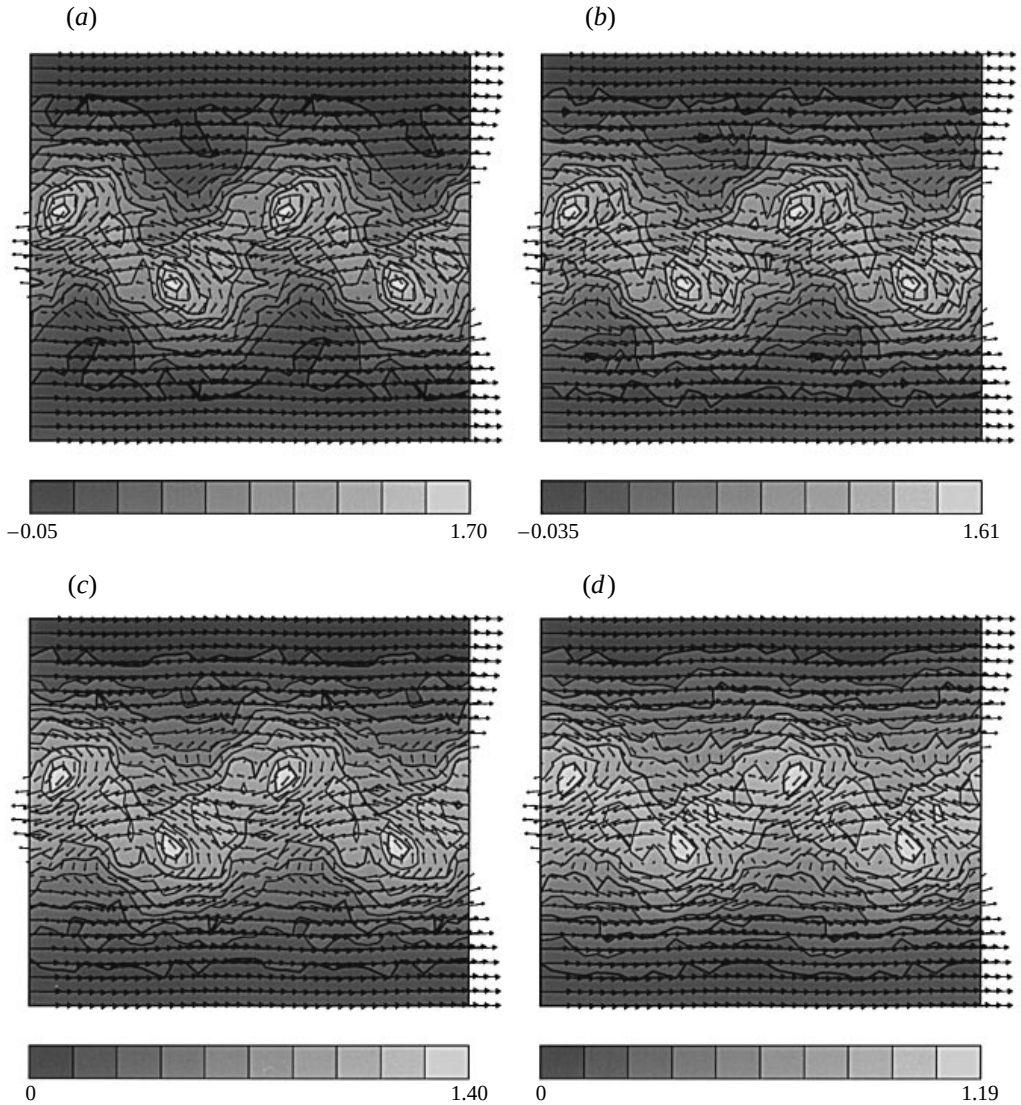

FIGURE 18. Contours of phase-averaged surrogate SGS dissipation $-\frac{15}{2}\langle\tau_{11}\widetilde{S}_{11}\rangle_c$, normalized with the centreline dissipation ε_{CL}. Results are for a Gaussian filter. (*a*) $\Delta/\eta = 300$, (*b*) $\Delta/\eta = 200$, (*c*) $\Delta/\eta = 100$, (*d*) $\Delta/\eta = 50$. As in figure 17 and in all subsequent figures, vectors correspond to phase-averaged velocity.

6.5. *Phase-averaged SGS dissipation*

The phase-averaged SGS dissipation is now measured, using the single-wire data. As before, subgrid-scale isotropy is assumed to hold also for the conditionally averaged statistics, so that we evaluate the surrogate SGS dissipation according to

$$\left\langle \tau_{ij}\widetilde{S}_{ij}\right\rangle_c \approx \tfrac{15}{2}\left\langle \tau_{11}\widetilde{S}_{11}\right\rangle_c. \tag{36}$$

Results are shown in figure 18, normalized with the global viscous dissipation ε_{CL} at the centreline. The different plots are for different filter sizes, from $\Delta/\eta = 300$ down to 50. The first conclusion that can be drawn from these results is that there is a clear

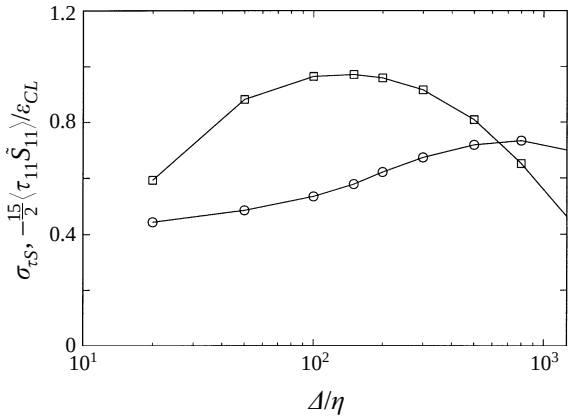

FIGURE 19. Circles: degree of spatial non-uniformity of phase-averaged surrogate dissipation rate along Φ, as a function of filter width. This non-uniformity is quantified by means of the root-mean-square value at $y/\ell = 0.88$. Also shown (squares) is the global mean value of the surrogate SGS dissipation at $y/\ell = 0.88$, showing an approximate plateau near ε_{CL}, characteristic of an inertial range.

correlation, or effect, of the coherent structure on the surrogate SGS dissipation field. At any fixed y/ℓ there are marked changes along the phase. While the peaks in overall mean SGS dissipation were located at the centreline, the peaks in phase-averaged dissipation are at the height of the roll centres. However, the peaks are concentrated at the roll fronts, not their centres. It is tempting to raise the possibility that this is related to secondary structures (ribs). The ribs are believed (see HH) to be stretched by the saddle and then merge with the spanwise rolls at about the location where the surrogate SGS dissipation peaks are located. It is quite possible that such merging is associated with strong transfer of energy from large to small scales (or SGS dissipation).

Such an interpretation must be tempered with a reminder of the strong assumptions that underlie the analysis (SGS isotropy and one-dimensional filtering). However, at the very least we may conclude that there is a strong effect of coherent structure on the subgrid dynamics. If SGS isotropy holds, then the results imply that there is a strong effect on the SGS dissipation. If SGS isotropy does not hold, then the results imply that there is a strong effect on the 1-1 component, and on small-scale anisotropy.

Another observation in figure 18 is that the distributions appear to become more uniform in the horizontal (streamwise) direction as the filter size decreases. An important element in the Kolmogorov phenomenology of the turbulence energy cascade is that small scales become independent of large scales as the scale ratio increases. In the present context, if the SGS scales were independent of large-scale phenomena, one would expect uniform distributions of the phase-averaged SGS dissipation in the streamwise direction. In order to quantify the spatial non-uniformity of SGS dissipation, the root-mean-square of $-\frac{15}{2}\langle\tau_{11}\widetilde{S}_{11}\rangle_c$ is computed over x (or phase Φ), at a fixed y-location. Such an r.m.s., σ, can be computed for various filter lengths according to

$$\sigma^2 = \frac{m\sum_{i=1}^{m}\left(-\frac{15}{2}\langle\tau_{11}\widetilde{S}_{11}|\Phi_i\rangle_c\right)^2 - \left(\sum_{i=1}^{m}\left(-\langle\frac{15}{2}\tau_{11}\widetilde{S}_{11}|\Phi_i\rangle_c\right)\right)^2}{m(m-1)}, \tag{37}$$

where $m = 20$ bins. The y-location is $y/\ell = 0.88$, where $\langle\omega_3\rangle_c$ is maximum. The

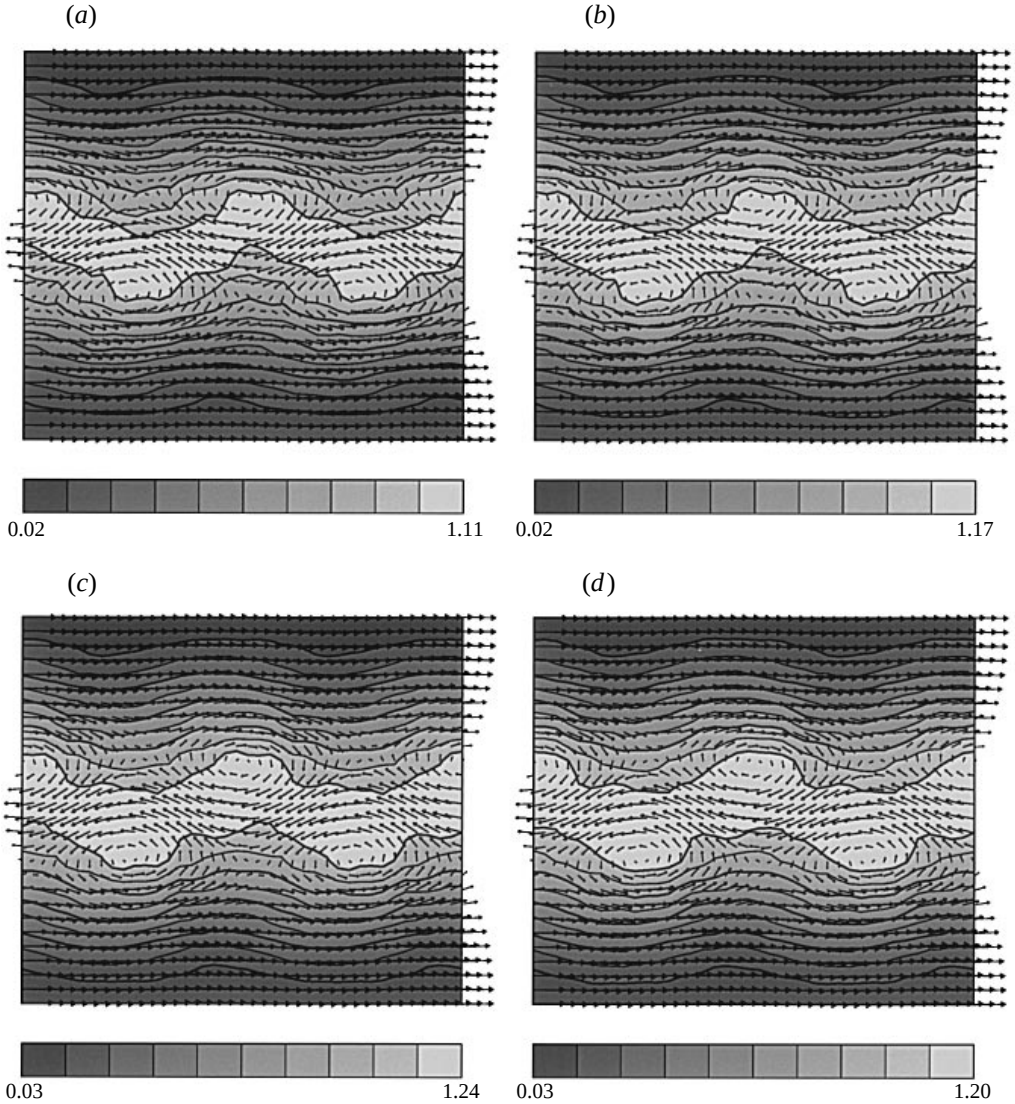

FIGURE 20. Contours of phase-averaged surrogate Smagorinsky dissipation $15^{3/2}(0.06\Delta)^2\langle|\widetilde{S}_1 1|^3\rangle_c$, normalized with the centreline dissipation ε_{CL}. Results are for a Gaussian filter. (*a*) $\Delta/\eta = 300$, (*b*) $\Delta/\eta = 200$, (*c*) $\Delta/\eta = 100$, (*d*) $\Delta/\eta = 50$.

results are shown in figure 19. The mean value $-\frac{15}{2}\langle\tau_{11}\widetilde{S}_{11}\rangle$ is superimposed on the same figure. With an order of magnitude change in Δ (say between $\Delta = 800\eta$ and 80η), there is only a 30% decrease in the spatial r.m.s. of SGS dissipation, in the phase-averaged contours. This result shows that the approach to independence of large and small scales, if it exists, is surprisingly slow. In agreement with the findings of Piomelli *et al.* (1996) in channel flow, we conclude that there is a strong correlation between coherent flow structures at large scales and SGS dissipation at much smaller scales.

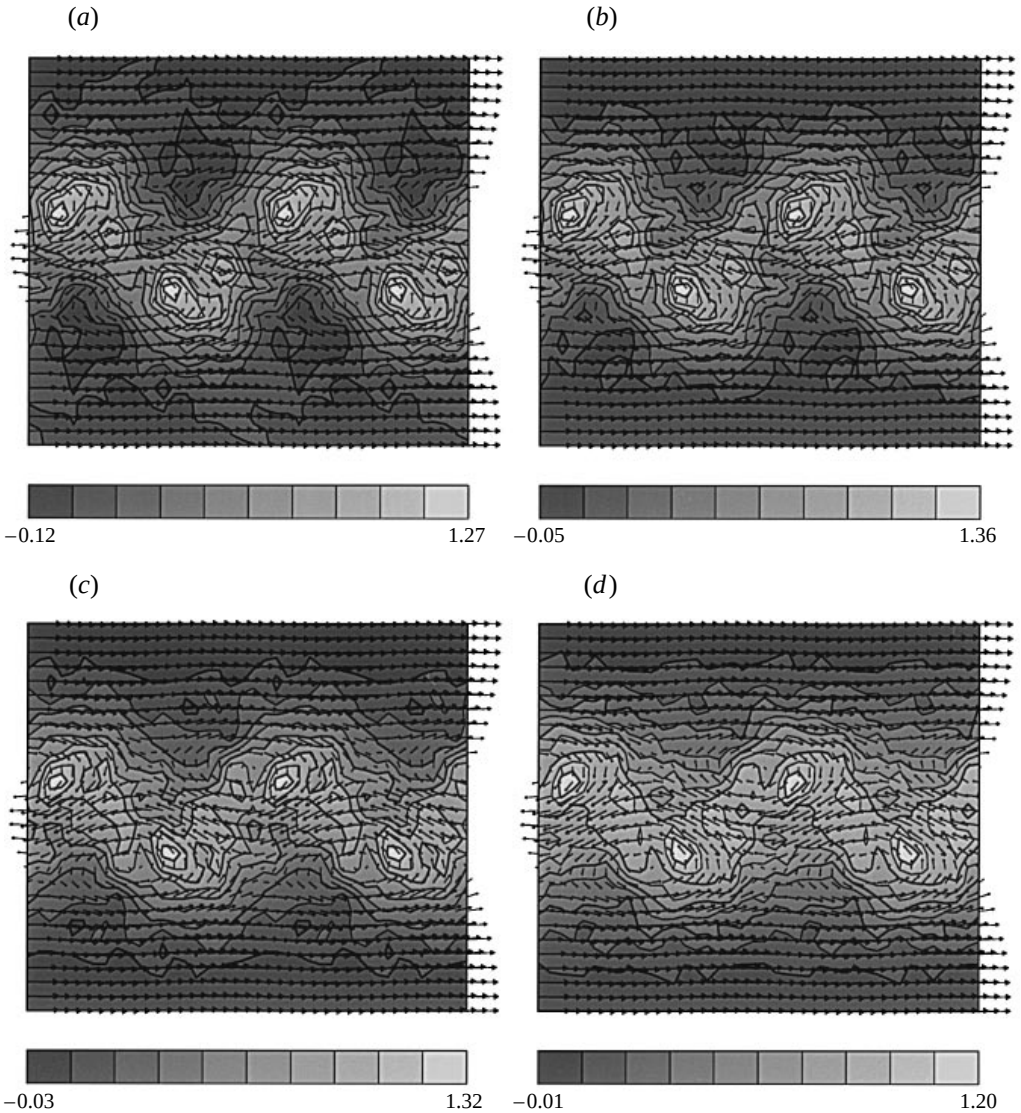

FIGURE 21. Contours of phase-averaged surrogate dissipation of the similarity model, $-\frac{15}{2}\langle L_{11}\widetilde{S}_{11}\rangle_c$, normalized with the centreline dissipation ε_{CL}. Results are for a Gaussian filter. (*a*) $\Delta/\eta = 300$, (*b*) $\Delta/\eta = 200$, (*c*) $\Delta/\eta = 100$, (*d*) $\Delta/\eta = 50$.

6.6. *Phase-averaged models of SGS dissipation*

Next, the properties of SGS models are examined. The energy dissipation produced by the Smagorinsky model, using (23) but phase-averaged, is shown in figure 20 for different filter sizes. A constant Smagorinsky coefficient of $C_S = 0.06$ was used, based on the globally averaged results of §4.2. Clearly, the distribution is quite different from the distribution of the SGS dissipation in figure 18. The peak values are more uniformly distributed along the centreline, with some preference towards the roll centres as opposed to their fronts. Thus, the presence of rollers appears to have a much weaker effect on fluctuating strain (which enters directly in the Smagorinsky model) than on the real nonlinear energy transfer.

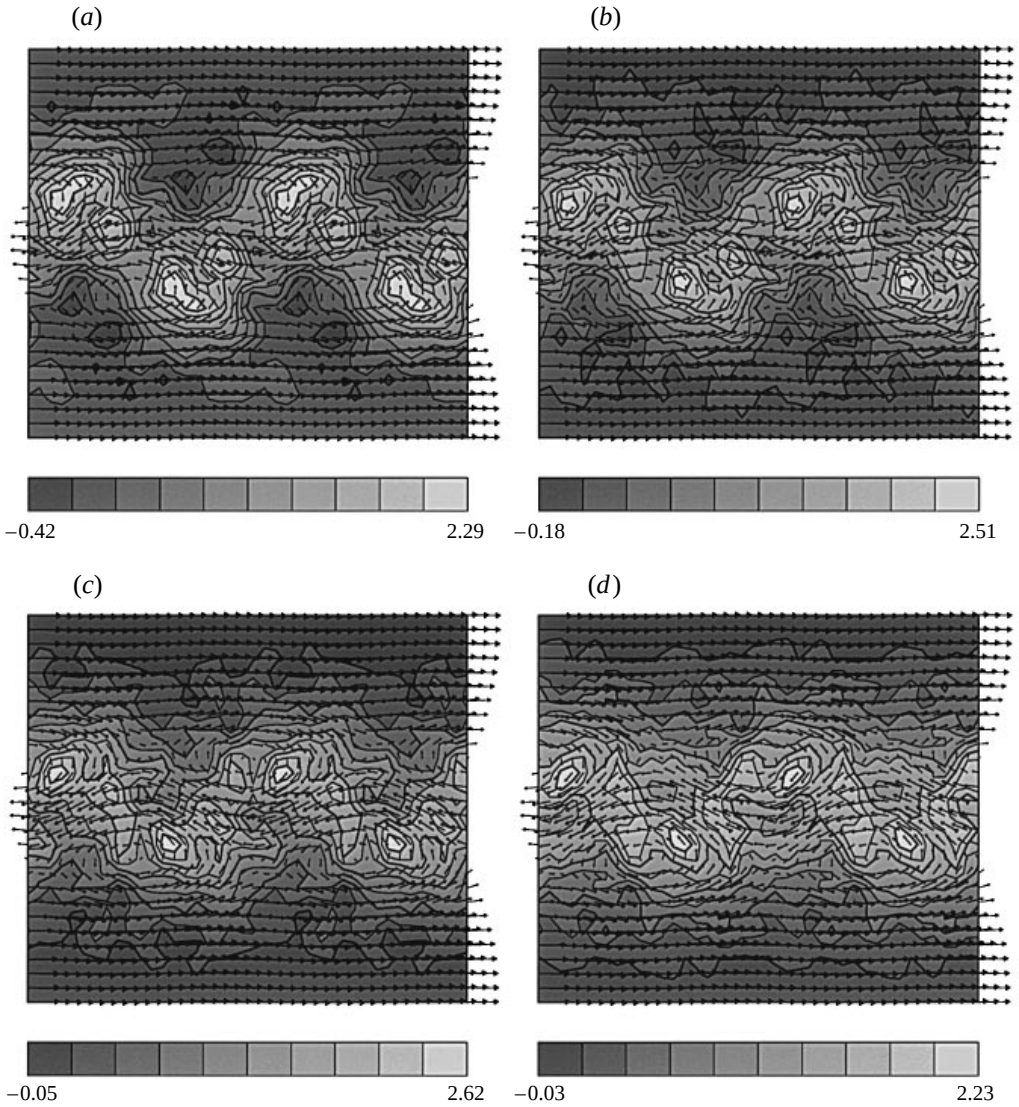

FIGURE 22. Contours of phase-averaged surrogate dissipation predicted by the dynamic Smagorinsky model, $15^{3/2}(\Delta^2\langle L_{11}M_{11}\rangle_c/\langle M_{11}M_{11}\rangle_c)\ \langle|\widetilde{S}_{11}|^3\rangle_c$, normalized with the centreline dissipation ε_{CL}. Results are for a Gaussian filter. (*a*) $\Delta/\eta = 300$, (*b*) $\Delta/\eta = 200$, (*c*) $\Delta/\eta = 100$, (*d*) $\Delta/\eta = 50$.

The phase-averaged SGS dissipation using the similarity model is shown in figure 21. A value $C_L = 1.0$ is used. As can be seen by comparing these distributions with figure 18, the similarity model captures the qualitative features of the real distribution much better than the Smagorinksy model. The spatial agreement with the actual SGS dissipation is quite good with regions of peak forward scatter agreeing both in terms of location and up to about 20% in intensity. This also agrees with the findings of Piomelli *et al.* (1996) who found more realistic conditional flow structures based on the similarity model than based on the Smagorinsky model.

The dynamic Smagorinsky model is investigated next, again at various filter lengths between $\Delta = 50\eta$ and 300η. We measure a conditional dynamic coefficient by phase

averaging the numerator and denominator in (26). The predicted conditional SGS dissipation is then obtained according to

$$-15^{3/2}\Delta^2\,\frac{\langle L_{11}\widetilde{S}_{11}\rangle_c}{\langle M_{11}M_{11}\rangle_c}\,\langle|\widetilde{S}_{11}|^3\rangle_c. \tag{38}$$

Results are shown in figure 22, and are normalized by ε_{CL}. Comparing to the actual SGS dissipation in figure 18 shows a qualitative resemblance. However, when comparing magnitudes, there are discrepancies: about 50% too much dissipation in the front of the rolls, and too much backscatter in the outer part of the wake. In §4.4 it was found that the dynamic model (evaluated with the present assumptions and one-dimensonal simplifications) gave a 25% overestimate of the global coefficient. A significant discrepancy in conditional averages is therefore not too surprising. Nevertheless, we can conclude that the qualitative features of the real SGS dissipation are reproduced much better with the dynamic model than with the regular Smagorinsky model.

6.7. *Similarity model with cutoff filter*

It is well known that the correlation coefficient between the actual SGS stress and the similarity model is high when using Gaussian and top-hat filters (well localized in physical space), but is very low when using a cutoff filter in wave space (see e.g. Liu *et al.* 1994). In that reference, this effect was attributed to 'ringing', namely spatial oscillations that arise due to Gibbs phenomenon when filtering spatially local structures with a cutoff filter. While this argument is plausible in explaining the low correlation displayed by the cutoff-filtered similarity model during *a priori* tests, the question remains whether there is any support for the similarity model if a cutoff filter is used, as would be the case in a spectral simulation.

The phase-averaged dissipation predicted by the similarity model using cutoff filters is examined, and is compared with the real dissipation where the stress and strain rate are also evaluated using the cutoff filter. The comparison is performed at filter lengths of $\Delta = 200\eta$ and 50η. Figure 23 displays the results, again normalized by ε_{CL}. At larger filter sizes the results are quite comparable to those of the Gaussian filter, although the SGS magnitudes are slightly larger at the peaks. The same is true at $\Delta = 50\eta$, except for the fact that some additional oscillations (jitter) can be discerned in the contours. Also, there are more discrepancies between the modelled and real SGS dissipation than for the case of Gaussian filter shown in figure 18. Nevertheless, the qualitative features of the conditional SGS dissipation are still reproduced. The model predicts local peaks of forward SGS dissipation at the roll fronts. From the point of view of phase-averaged SGS dissipation, this result suggests that the similarity modelling approach has merit (at least over the plain Smagorinsky model) even when dealing with spectral cutoff filters.

6.8. *Phase-decomposed SGS dissipation*

In the previous section, the dissipation of the entire resolved kinetic energy field was studied with phase averaging. In this section, the resolved field is first phase decomposed to exclude the coherent field from the interaction between resolved and unresolved scales.

The phase-averaged SGS dissipation may be decomposed as follows:

$$-\langle\tau_{ij}\widetilde{S}_{ij}\rangle_c = -\left(\langle\tau_{ij}\rangle_c\langle\widetilde{S}_{ij}\rangle_c + \langle\tau'_{ij}\widetilde{S}'_{ij}\rangle_c\right), \tag{39}$$

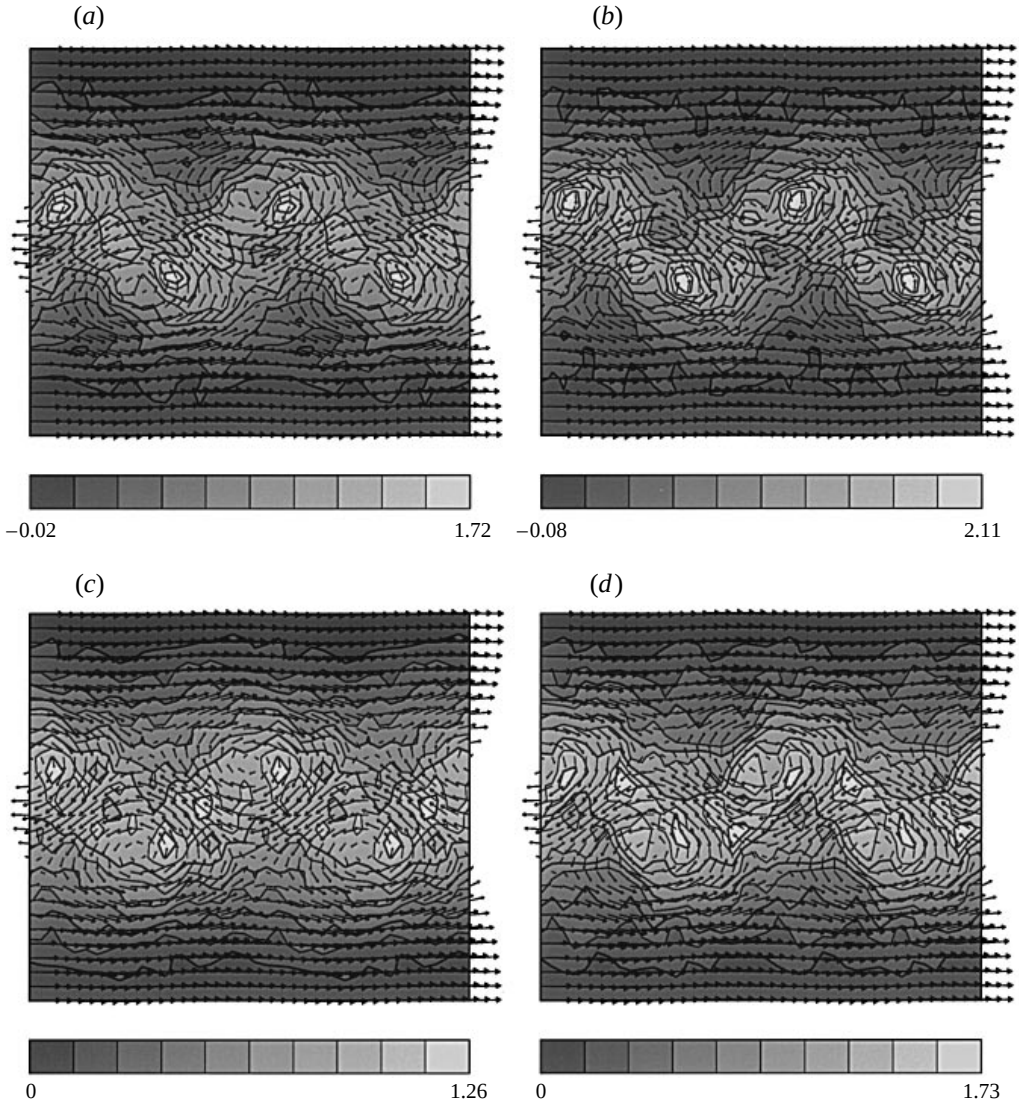

FIGURE 23. Contours of phase-averaged surrogate SGS dissipation using the sharp cutoff instead of Gaussian filter. (*a*) Real dissipation $-\frac{15}{2}\langle\tau_{11}\widetilde{S}_{11}\rangle_c$ at $\Delta/\eta = 200$. (*b*) Dissipation predicted by similarity model at $\Delta/\eta = 200$ with spectral cutoff filter. (*c*) Real dissipation at $\Delta/\eta = 50$. (*d*) Similarity model with cutoff filter at $\Delta/\eta = 50$.

where $\tau'_{ij} = \tau_{ij} - \langle\tau_{ij}\rangle_c$ and $\widetilde{S}'_{ij} = \widetilde{S}_{ij} - \langle\widetilde{S}_{ij}\rangle_c$. The first term in (39) may be interpreted as the energy that is transferred from (or to) the coherent field towards (or from) the subgrid scales, while the second represents energy transferred between all remaining resolved scales and the SGS range.

To see more clearly that $-\langle\tau_{ij}'\widetilde{S}'_{ij}\rangle_c$ is indeed the energy dissipation from resolved, but incoherent, motion to unresolved motion, an incoherent resolved kinetic energy equation is derived, following Reynolds & Hussain (1972). Denoting the incoherent part of the velocity as $\widetilde{u}'_i$, one may define the incoherent, but resolved, kinetic energy

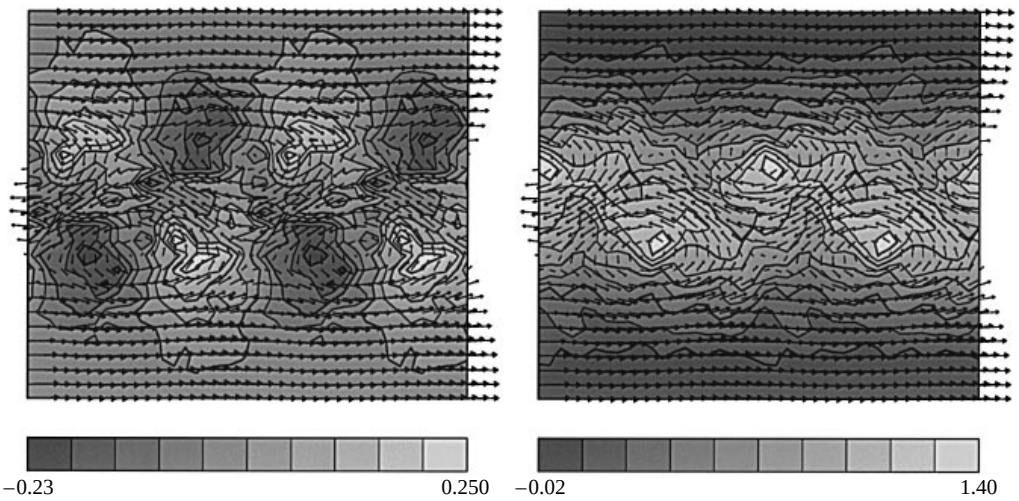

FIGURE 24. Contours of phase-decomposed surrogate SGS dissipation. (*a*) Contribution from coherent part, $-\frac{15}{2}\langle\tau_{11}\rangle_c\langle\widetilde{S}_{11}\rangle_c$, corresponding to energy flux between the coherent field and the subgrid scales. (*b*) Energy flux between incoherent (but resolved) field and subgrid scales, $-\frac{15}{2}\langle\tau_{11}{}'\widetilde{S}'_{11}\rangle_c$. Results are for Gaussian filter, at $\Delta/\eta = 200$.

according to

$$\tfrac{1}{2}\widetilde{e}^2 = \tfrac{1}{2}\widetilde{u}'_i\widetilde{u}'_i. \tag{40}$$

One starts with the resolved momentum equation for the total filtered velocity $\widetilde{u}_i$. Then, all of the primitive variables including the SGS stress are decomposed into a coherent and incoherent part. A second equation is formed by phase averaging and the difference is taken to obtain an equation for the incoherent resolved velocity:

$$\frac{\partial\widetilde{u}'_i}{\partial t} + \langle\widetilde{u}_j\rangle_c\frac{\partial\widetilde{u}'_i}{\partial x_j} = -\frac{\partial}{\partial x_j}\left(\frac{\widetilde{p}'}{\rho}\delta_{ij} - \langle\widetilde{u}'_i\widetilde{u}'_j\rangle_c + \widetilde{u}'_i\widetilde{u}'_j + \langle\widetilde{u}'_i\rangle_c\widetilde{u}'_j + \tau_{ij}{}' - 2\nu\widetilde{S}'_{ij}\right). \tag{41}$$

Multiplying by $\widetilde{u}'_i$, phase averaging, neglecting the viscous dissipation, and not writing the transport term in detail yields

$$\frac{\partial}{\partial t}\langle\tfrac{1}{2}\widetilde{e}^2\rangle_c + \langle\widetilde{u}_j\rangle_c\frac{\partial}{\partial x_j}\langle\tfrac{1}{2}\widetilde{e}^2\rangle_c = -\langle\widetilde{u}'_i\widetilde{u}'_j\rangle_c\langle\widetilde{S}_{ij}\rangle_c + \langle\tau_{ij}{}'\widetilde{S}'_{ij}\rangle_c - \frac{\partial}{\partial x_j}\langle\ldots\rangle_c. \tag{42}$$

The term $-\langle\widetilde{u}'_i\widetilde{u}'_j\rangle_c\langle\widetilde{S}_{ij}\rangle_c$ is the production of resolved incoherent kinetic energy due to coherent strain (or dissipation of coherent energy due to resolved incoherent motion). The term $\langle\tau_{ij}{}'\widetilde{S}'_{ij}\rangle_c$ is indeed the sink (if negative) of resolved, but incoherent, kinetic energy due to the SGS stress.

Next, phase-averaged distributions of $-\frac{15}{2}\langle\tau_{11}\rangle_c\langle\widetilde{S}_{11}\rangle_c$ and $-\frac{15}{2}\langle\tau_{11}{}'\widetilde{S}'_{11}\rangle_c$ are evaluated and shown in figure 24. The filter size was $\Delta = 200\eta$, using a Gaussian filter. It is interesting to note that the levels of the coherent part reach only 16% of the peak total dissipation (in figure 18), which while not negligible, is not a dominant effect. The incoherent SGS dissipation $-\frac{15}{2}\langle\tau'_{11}\widetilde{S}'_{11}\rangle_c$ is shown in figure 24(*b*). Compared to figure 18, one can see that there is less streamwise modulation by the coherent structures, especially near the outer edges of the wake where the contour lines are more horizontal. Nevertheless, near the centreline, the contours still display significant

modulation. The peak still occurs near the roll fronts, but closer to their centre than the peaks of full SGS dissipation.

We conclude that there are significant effects of the coherent structure on the SGS dissipation, even when only considering the incoherent portion of this variable.

7. Summary and conclusions

The primary motivation of this work is to supplement existing numerical *a priori* and *a posteriori* studies of the SGS stress and models with *a priori* experimental results at high Reynolds numbers, in a fairly complex flow field with outer intermittency and regions of coherent structure.

The first part of the study involved globally averaged quantities across the wake of a cylinder, at four downstream locations. Owing to the need to maximize the turbulence Reynolds number, a fairly large cylinder was chosen leading some features of the downstream development of the wake (e.g. r.m.s. velocities) to exceed those of a canonical free wake.

Based on the measurements, comparisons were made between the actual and modelled mean SGS dissipation. Also, the coefficients of the Smagorinsky and similarity models, as well as those obtained from the dynamic Smagorinsky model were measured. The surrogate dissipation rate profiles from $x/D = 25$ to 100 agreed out to the wake half-width, ℓ, when scaled with the centreline total dissipation rate. For $y > \ell$, the profiles for lower x/D decayed more slowly. When corrected for the effects of one-dimensional filtering, the measured Smagorinsky coefficient fell inside the expected range of 0.1 to 0.12. The viability of the Smagorinsky model was confirmed by showing that the constancy of C_S was relatively insensitive to variations of the Reynolds number, filter length, and downstream location. A weak cross-stream decrease of C_S was observed for filter scales above $\sim 0.01L_1$, meaning that the constant-coefficient Smagorinsky model slightly overpredicts SGS dissipation in the outer wake, unless filter scales are about two or more orders of magnitude smaller than the integral scale. This trend is reminiscent of the well-known overprediction of the $-\overline{u'v'}$ Reynolds stress using the mixing-length model in the plane wake. However, conditional averaging based on outer intermittency to eliminate possible effects of non-turbulent patches did not significantly affect this trend. This leads to the conclusion that the weak decrease in C_S is not due to outer intermittency but to an inherent difference in the structure of turbulence, or to anisotropy effects which we could not capture with the instrumentation, the surrogate dissipation, and limitations of one-dimensional filtering.

The similarity model was insensitive to changes in downstream distance, Reynolds number, and filter length, as long as both Δ and 2Δ remained well inside the inertial range. As expected, the correlation for the similarity model was considerably higher than the Smagorinsky model. The dynamic Smagorinsky coefficient was found to be 25% higher than the traditional Smagorinsky coefficient, but agreed with its basic trends of a slight decline in the outer part of the wake.

Following the analysis of globally averaged variables, the interaction of coherent structure and the dynamics of the subgrid motion were studied. The presence of large-scale coherent structures was shown to strongly affect the distribution of the measured surrogate for SGS energy dissipation. This was the case even after phase decomposing the SGS stress and strain rates, to extract the coherent part of the field. The surrogate SGS dissipation structure was found to become more evanescent with decreasing filter size, though much of the structure remained even at the small-scale

end of the inertial range, $\Delta = 20\eta$. This trend suggests that to reach independence between large and small scales requires very large scale separations. It is important to recall again that the observed changes in surrogate dissipation due to coherent structures may not only reflect the actual distribution of SGS dissipation, but could also reflect varying deviations from the assumed SGS isotropy. At any rate, our results clearly show that the coherent structures have a direct effect on SGS dynamics, either in terms of true SGS dissipation or SGS anisotropy (or a combination of both).

The Smagorinsky model was unable to reproduce the observed distribution of surrogate SGS dissipation with respect to the coherent structures, while the similarity model captured the main features as long as the filters were inside the inertial range. The dynamic Smagorinsky model, with the coefficient obtained from phase averaging, did reproduce qualitative features of the (surrogate) SGS dissipation. The similarity model with spectral cutoff filtering showed essentially zero correlation with the real stress field, but did display the main characteristics of the structure of surrogate SGS dissipation.

An important as yet unresolved question is what happens further downstream (i.e. at $x/D > 50$) when the organized Kármán vortex street disappears. It is believed that there still are 'coherent structures' but that they are no longer nicely periodic, i.e. they are not discernible from phase averaging. How much of present results carry over to the relationship between such non-periodic large-scale structures and the subgrid scales is not known, and clearly deserves further study.

In summary, present results provide detailed evidence that SGS modelling based on 'learning' from resolved scales (such as in the dynamic or similarity models) should lead to more realistic predictions than the constant-coefficient eddy-viscosity model, when turbulence is spatially complex and when coherent structures affect the SGS dynamics directly. At the level of phase-averaged dissipation, both the dynamic Smagorinsky and the similarity models appeared to work well, so that any linear combination of the two should also provide a good model to reproduce phase-averaged dissipation. In recent years, such mixed models have shown promise in LES (e.g. Zang *et al.* 1993; Wu & Squires 1995; Vreman *et al.* 1994). The mixed model is also advantageous to model the response of SGS turbulence to rapid distortion (Liu *et al.* 1997).

We thank Professors O. Knio and N. Jones for useful comments and discussions. This work was funded by the National Science Foundation (grant CTS-9408344) and the Office of Naval Research (grant N00014-92-J-1109). Data analysis and management were done mostly on an in-house PowerChallenge L supported by NSF (grant CTS-9506077). Some initial analysis was done at the Pittsburgh Supercomputing Center.

REFERENCES

Adrian, R. J. 1991 Particle-imaging techniques for experimental fluid mechanics. *Ann. Rev. Fluid Mech.* **23**, 261–304.

Antonia, R. & Atkinson J. 1974 Use of a pseudo-turbulent signal to calibrate an intermittency measuring circuit. *J. Fluid Mech.* **64**, 679–699.

Bardina, J., Ferziger, J. & Reynolds, W. C. 1980 Improved subgrid scale models for large eddy simulation. *AIAA Paper* 80-1357.

Brown, G. & Roshko, A. 1974 On density effects and large structure in turbulent mixing layers. *J. Fluid Mech.* **64**, 775–815.

Cantwell, B. 1981 Organized motion in turbulent flow. *Ann. Rev. Fluid Mech.* **13**, 457–515.

Cantwell, B. & Coles, C. 1983 An experimental study of entrainment and transport in the turbulent near wake of a circular cylinder. *J. Fluid Mech.* **136**, 321–374.

Chen, C. & Blackwelder, R. 1978 Large scale motion in a boundary layer: a study using temperature contamination. *J. Fluid Mech.* **89**, 1–32.

Clark, R. G., Ferziger, J. H. & Reynolds, W. C. 1979 Evaluation of subgrid models using an accurately simulated turbulent flow. *J. Fluid Mech.* **91**, 1–16.

Comte-Bellot, G. & Corrsin, S. 1966 The use of a contraction to improve the isotropy of grid generated turbulence. *J. Fluid Mech.* **25**, 657–682.

Cook, A. W. 1997 Determination of the constant coefficient in scale similarity models of turbulence. *Phys. Fluids* **9**, 1485–1487.

Corrsin, S. 1943 *Tech. Rep.* W-94. NACA Wartime Report.

Corrsin, S. & Kistler, A. 1955 *Tech. Rep.* 1244. NACA Report.

Crow, C. & Champagne, F. 1971 Orderly structure in jet trubulence. *J. Fluid Mech.* **48**, 547–591.

Deardorff, J. W. 1970 A numerical study of three-dimensional turbulent channel flow at large Reynolds numbers. *J. Fluid Mech.* **41**, 453–480.

Domaradski, J. A., Liu, W. & Brachet, M. E. 1993 An analysis of subgrid-scale interactions in numerically simulated isotropic turbulence. *Phys. Fluids* A **5**, 1747–1759.

Germano, M., Piomelli, U., Moin, P. & Cabot, W. H. 1991 A dynamic subgrid-scale eddy viscosity model. *Phys. Fluids* A **3**, 1760–1765.

Ghosal, G., Lund, T., Moin, P. & Akselvoll, K. 1995 A dynamic localization model for large-eddy simulation of turbulent flows. *J. Fluid Mech.* **286**, 229–255.

Härtel, C., Kleiser, L., Unger, F. & Friedrich, R. 1994 Subgrid-scale energy transfer in the near-wall region of turbulent flows. *Phys. Fluids* **6**, 3130–3143.

Hedley, T. & Keffer, J. 1974 Turbulent/non-turbulent decisions in an intermittent flow. *J. Fluid Mech.* **64**, 625–644.

Hussain, F. & Hayakawa, M. 1987 Eduction of large-scale organized structures in a turbulent plane wake. *J. Fluid Mech.* **180**, 193–229 (referred to herein as HH).

Kollman, K. 1982 Intermittent turbulent flow. In *Frontiers in Fluid Mechanics* (ed. S. Davis & J. Lumley), pp. 88–112. Springer.

Kovasznay, L., Kibens, V. & Blackwelder, R. 1970 Large-scale motion in the intermittent region of a turbulent boundary layer. *J. Fluid Mech.* **41**, 283–325.

Kraichnan, R. H. 1976 Eddy viscosity in two and three dimensions. *J. Atmos. Sci.* **33**, 1521–1536.

Leonard, A. 1974 Energy cascade in large-eddy simulations of turbulent fluid flows. *Adv. Geophys.* **18**, 237–248.

Lesieur, M. & Metais, O. New trends in large-eddy simulations of turbulence. *Ann. Rev. Fluid Mech.* **28**, 45–82.

Leslie, D. C. & Quarini, G. L. 1979 The application of turbulence theory to the formulation of subgrid modelling procedures. *J. Fluid Mech.* **91**, 65–91.

Lilly, D. K. 1967 The representation of small-scale turbulence in numerical simulation experiments. In *Proc. IBM Sci. Comput. Symp.,* pp. 195–209.

Liu, S., Katz, J. & Meneveau, C. 1997 Evolution and modelling of subgrid scales during rapid straining of turbulence (submitted).

Liu, S., Meneveau, C. & Katz, J. 1994 On the properties of similarity subgrid-scale models as deduced from measurements in a turbulent jet. *J. Fluid Mech.* **275**, 83–119.

Liu, S., Meneveau, C. & Katz, J. 1995 Experimental study of similarity subgrid-scale models of turbulence in the far-field of a jet. *Appl. Sci. Res.* **54**, 177–188.

Matsumura, M. & Antonia, R. A. 1993 Momentum and heat transport in the turbulent intermediate wake of a circular cylinder. *J. Fluid Mech.* **250**, 651–668.

Meneveau, C. 1994 Statistics of turbulence subgrid-scale stresses: Necessary conditions and experimental tests. *Phys. Fluids* **6**, 815–833.

Meneveau, C., Lund, T. & Cabot, W. 1996 A Lagrangian dynamic subgrid-scale model of turbulence. *J. Fluid Mech.* **319**, 353–386.

Monin, A. & Yaglom, A. 1971 *Statistical Fluid Mechanics.* MIT Press.

Muck, K. C. 1980 Comparison of various schemes for the generation of the turbulent intermittency function. *Imperial College Aero Rep.* 80-03.

MURLIS, J. & BRADSHAW, P. 1974 On the measurement of intermittency in turbulent flow. *Imperial College Aero. Rep.* 74-04.

MURRAY, J., PIOMELLI, U. & WALLACE, J. 1996 Spatial and temporal filtering of experimiental data for a priori studies of subgrid-scale stresses. *Phys. Fluids* **8**, 1978–1980.

O'NEIL, J. 1996 Subgrid-scale stresses and their modelling in the turbulent plane wake. PhD thesis, The Johns Hopkins University.

OSTER, D. & WYGNANSKI, I. 1982 The forced mixing layer between parallel streams. *J. Fluid Mech.* **123**, 91–130.

PIOMELLI, U., CABOT, W., MOIN, P. & LEE, S. 1991 Subgrid-scale backscatter in turbulent and transitional flows. *Phys. Fluids* A **3**, 1766.

PIOMELLI, U., MOIN, P. & FERZIGER, J. H. 1988 Model consistency in large eddy simulation of turbulent channel flows. *Phys. Fluids* **31**, 1884.

PIOMELLI, U., YU, Y. & ADRIAN, R. 1996 Subgrid-scale energy transfer and near-wall turbulence structure. *Phys. Fluids* **8**, 215–224.

PRESS, W. H., TEUKOLSKY, S. A., VETTERLING, W. T. & FLANNERY, B. P. *Numerical Recipes*, 2nd edn. Cambridge University Press.

REYNOLDS, W. C. & HUSSAIN, F. 1972 The mechanics of an organized wave in turbulent shear flow. Part 3. Theoretical models and comparisons with experiments. *J. Fluid Mech.* **54**, 263–288.

ROGALLO, R. & MOIN, P. 1984 Numerical simulation of turbulent flows. *Ann. Rev. Fluid. Mech.* **16**, 99.

ROSHKO, A. 1954 On the development of turbulent wakes from vortex streets. *Tech. Rep.* TN 1191. NACA.

SADDOUGHI, S. G. & VEERAVALLI, S. V. 1994 Local isotropy in turbulent boundary layers at high Reynolds number. *J. Fluid Mech.* **268**, 333–372.

SCOTTI, A., MENEVEAU, C. & LILLY, D. K. 1993 Generalized smagorinsky model for anisotropic grids. *Phys. Fluids* A **5**, 2306.

SMAGORINSKY, J. 1963 General circulation experiments with the primitive equations. i. the basic experiment. *Mon. Weath. Rev.* **91**, 99.

TENNEKES, H. & LUMLEY, J. L. 1972 *A First Course in Turbulence*. MIT Press.

TOWNSEND, A. 1956 *The Structure of Turbulent Shear Flow*. Cambridge University Press.

VREMAN,B., GEURTS, B. & KUERTEN, H. 1994 On the formulation of the dynamic mixed subgrid-scale model. *Phys. Fluids* A **6**, 4057–4059.

WU, X. & SQUIRES, K. 1995 Large eddy simulation of a canonical three-dimensional boundary layer. In *Proc. Tenth Symp. on Turbulent Shear Flows, Penn State* (ed. F. Durst, B. E. Launder, F. W. Schmidt & J. W. Whitelaw).

ZANG, Y., STREET, R. L. & KOSEFF, J. 1993 A dynamic mixed subgrid scale model and its application to rubulent recirculating flows. *Phys. Fluids* A **5**, 3186.